- Model validation and analyses of parameter sensitivity and uncertainty for
- modeling long-term retention and leaching of PFAS in the vadose zone
- Jicai Zeng¹, Mark L. Brusseau^{1,2}, Bo Guo^{1,*}
- ¹Department of Hydrology and Atmospheric Sciences, University of Arizona, Tucson, Arizona, USA
- ²Department of Environmental Science, University of Arizona, Tucson, Arizona, USA
- *Corresponding author: Bo Guo, <u>boguo@arizona.edu</u>

Abstract

7

8

9

10

11

12

13

14

15

16

17

18

19

20

21

22

23

24

25

26

27

PFAS are emerging contaminants widespread in the environment. As surfactants, PFAS tend to accumulate at solid-water and air-water interfaces in the vadose zone, which may pose long-term threats to groundwater. The primary factors that control the long-term retention of PFAS in the vadose zone remain poorly understood. To address this knowledge gap, we first use multiple datasets from transport experiments to validate a state-of-the-art mathematical model that incorporates transient variably saturated flow, surfactant-induced flow, and rate-limited and nonlinear solid-phase and air-water interfacial adsorption. We then employ the validated model to simulate and analyze the primary processes and parameters controlling the retention and leaching of PFAS in the vadose zone at a model fire-training-area site. Our simulations show that adsorption at solid-water and air-water interfaces leads to strong retention of PFAS in the vadose zone. The strength of retention increases with PFAS chain length and porewater ionic strength, while it decreases at greater PFAS concentrations due to nonlinear adsorption. Comprehensive parameter sensitivity analyses reveal that model predictions are most sensitive to parameters related to the air-water interfacial area and PFAS interfacial properties when air-water interfacial adsorption (AWIA) is more important than solid-phase adsorption (SPA). Predicted PFAS leaching rates vary by a wide range resulting from uncertainties in the input parameters, but the uncertainty range is much greater for longer-chain PFAS than that of their shorter-chain counterparts. The simulated arrival times to groundwater were found to follow log-normal distributions. Finally, model complexity analysis reveals that nonlinearity in AWIA and kinetic SPA and kinetic AWIA have a minimal impact on the long-term retention of PFAS under the wide range of field conditions examined in the present study.

- Keywords: Leaching; interfacial adsorption; variably saturated flow; PFAS; uncertainty; kinetic
- 28 adsorption

1 Introduction

Per- and polyfluoroalkyl substances (PFAS) are synthetic chemicals widely used in industrial applications and commercial products due to their unique physicochemical properties. Over 4,000 PFAS have been on the global market since the 1940s (Cousins et al., 2020; OECD, 2018). PFAS may be released to the environment through various sources including fire training area (FTA) and other sites that use aqueous film-forming foams (AFFFs) (Anderson et al., 2019; Hatton et al., 2018), industrial sites that manufacture or use PFAS products, landfills and wastewater treatment plants, and agricultural lands that receive biosolids (ITRC, 2018). Most PFAS are surfactants (Kissa, 2001), and as a result, they tend to adsorb at fluid-fluid interfaces, such as air—water interfaces in water-unsaturated soils. Despite the significant potential to affect human health, scientific investigations on the fate and transport of PFAS in the environment—especially in soils wherein multiple fluid phases and complex fluid-fluid interfaces coexist—have only begun recently. This topic has been deemed a critical research need (Naidu et al., 2020; SERDP, 2017; Sharifan et al., 2021; Sima & Jaffé, 2020; Simon et al., 2019).

A growing body of field investigations have demonstrated that the vadose zone can serve as significant source zones of PFAS to groundwater even several decades after the contamination events were stopped (e.g., Adamson et al., 2020; Anderson et al., 2019; Brusseau et al., 2020a; Dauchy et al., 2019; Filipovic et al., 2015; Høisæter et al., 2019; Sepulvado et al., 2011; Shin et al., 2011; Washington et al., 2010; Weber et al., 2017; Xiao et al., 2015). Field data revealed that the mass fraction of PFAS typically changes with depth and chain length (e.g., Brusseau et al., 2020a; Dauchy et al., 2019). The long-chain PFAS are generally dominant in the shallow vadose zone, while more short-chain PFAS are present at deeper depths, indicating that long-chain PFAS have stronger retention than their short-chain counterparts (Anderson et al., 2019; Baduel et al., 2017; Brusseau et al, 2020a; Casson & Chiang, 2018; Dauchy et al., 2019; Sepulvado et al., 2011; Washington et al., 2010). The large body of field evidence cited above demonstrates that PFAS experience strong retention in the vadose zone and the strength of retention varies among different PFAS. However, the mechanisms that control PFAS migration in the vadose zone especially

regarding the relative importance of adsorption at air—water interfaces and the primary controlling parameters for a large variety of PFAS with different physicochemical properties remain unclear.

54

55

56

57

58

59

60

61

62

63

64

65

66

67

68

69

70

71

72

73

74

75

76

77

78

The importance of air—water interfacial adsorption (AWIA) as a significant source of retention for PFOS and PFOA—two PFAS of primary concern—was assessed by Brusseau (2018) using surface tension data and laboratory-measured air-water interfacial areas. Several surface-tension-based analyses of AWIA covering a wider range of chain length and solution chemistry have since been reported (Brusseau, 2019a; Brusseau & Van Glubt, 2019; Costanza et al., 2019 & 2020; Schaefer et al., 2019a; Silva et al., 2019, 2021). These studies showed that chain length and solution ionic strength enhance AWIA of anionic PFAS. The impact of ionic strength, PFAS concentration, and porous media on AWIA has been examined by waterunsaturated miscible-displacement experiments using soil-packed columns (Brusseau et al., 2019b, 2021; Li et al., 2021; Lyu et al., 2018; Lyu et al., 2020; Lyu & Brusseau, 2020). These studies, employing steadystate flow conditions, demonstrated that AWIA is controlled by the interfacial behaviors of PFAS and soil hydraulic properties. However, time-dependent flow boundaries and transient variably saturated flow can lead to a rapid spatial and temporal evolution of air-water interfaces, which can then strongly influence the transport and retention of PFAS in the vadose zone. Additionally, like other surfactants (Bashir et al., 2018; Henry et al., 2001; Karagunduz et al., 2015; Smith & Gillham, 1994, 1999), PFAS dissolved in soil water can reduce surface tension and decrease capillary forces (i.e., surfactant-induced flow (SIF)), which in turn will influence unsaturated water flow and redistribute soil moisture. Finally, prior steady-state miscibledisplacement experiments demonstrated that while the adsorption at solid surfaces can be rate-limited, the adsorption at air-water interfaces can be mostly considered instantaneous under certain experimental conditions (Brusseau, 2020; Brusseau et al., 2021). Yet, it is unknown whether the kinetics remain insignificant under dynamic changes in water saturation and air-water interfacial area in vadose-zonerelevant conditions. The aforementioned complex coupled flow and transport processes need to be represented to understand and quantify the overall impact of AWIA on PFAS long-term retention under time-dependent infiltration fluxes in the vadose zone.

To date, only a few modeling studies on PFAS transport in the vadose zone have been reported. Shin et al. (2011, 2012) simulated PFOA transport in the vadose zone but did not consider AWIA. Guo et al. (2020) developed a new mathematical model that incorporates a comprehensive set of processes for PFAS transport and retention under transient variably saturated flow in the vadose zone. The model formulations account for SIF and nonlinear and rate-limited adsorption at the soil-water and air-water interfaces. Numerical simulations for a model AFFF-impacted FTA site demonstrated the importance of AWIA on PFAS retention in the vadose zone. For example, they showed that—depending on specific conditions such as soil properties and climatic conditions—the time scale for a majority of the PFOS plume to reach a depth of 5 m can be several decades. Silva et al. (2020) also reported a model that accounts for the processes discussed above (kinetic adsorption was not presented) and simulated PFAS transport in one and two dimensions. More recently, Zeng & Guo (2021) developed a three-dimensional mathematical model to investigate the impact of preferential flow and SIF on PFAS leaching in heterogeneous vadose zones. They suggested that compared to traditional contaminants, the acceleration of PFAS leaching due to preferential flow is further amplified by the destruction of air-water interfaces resulting from greater water saturations along the preferential flow pathways. Additionally, SIF was predicted to have a relatively minor impact on both the lateral spreading and long-term leaching of PFAS in the vadose zone even when PFAS are released at higher concentrations at AFFF-impacted sites. While the formulations of the above-discussed models are well-established, a thorough experimental validation of the coupled nonlinear processes, especially under transient flow conditions that are more relevant to field contamination sites, has not been reported in the literature.

79

80

81

82

83

84

85

86

87

88

89

90

91

92

93

94

95

96

97

98

99

100

101

102

103

104

Another critical aspect that has been minimally investigated is the relative importance of the various physicochemical processes and parameters controlling PFAS retention and leaching. As discussed above, multiple processes affect PFAS retention and their relative importance may change under different field conditions and for different PFAS. In addition, the mathematical models require a wide range of parameters for the properties and conditions for PFAS and the soil media in the vadose zone. It is of great importance to identify the primary processes and critical parameters that dominantly control the long-term leaching of

PFAS in the vadose zone, the insights from which will lead to improved quantitative predictions of PFAS leaching and provide practical guidance for managing and mitigating contamination risks at field sites.

To address the above-discussed challenges, (1) we use multiple experimental data sets (Brusseau, 2020; Karagunduz et al., 2015; Li et al., 2021; Lyu et al., 2018) to validate the mathematical model of Guo et al. (2020) for representing several important processes and conditions including SIF, solution chemistry, and nonlinear and kinetic solid-phase adsorption (SPA) and AWIA; (2) we then employ the validated model to conduct a series of simulations to investigate and analyze the primary factors controlling the leaching and retention of PFAS in the vadose zone under field conditions. Specifically, we simulate the transport of six representative PFAS at a model FTA site. The simulations consider a 30-year active-contamination period followed by a post-contamination period lasting 50 years or longer. A wide range of conditions are considered, including two climatic (semiarid vs. humid) conditions, two porous media (sand vs. soil), two different solution chemistries in porewater (deionized water (DIW) vs. synthetic groundwater (SGW)), and different applied concentrations of PFAS. These base simulations are then followed by comprehensive parameter sensitivity and uncertainty analyses that examined a total of 12 parameters that may control PFAS leaching in the vadose zone. Our analyses are guided by the following specific questions: what are the primary factors controlling the timescale of PFAS retention in the vadose zone? How does the timescale of retention change for different PFAS? And, what are the conditions under which AWIA or SPA become dominant retention processes?

2 Methodology

105

106

107

108

109

110

111

112

113

114

115

116

117

118

119

120

121

122

123

124

125

126

2.1 Mathematical model

We describe the variably saturated water flow in the vadose zone using the one-dimensional (1D) Richards equation (Richardson, 1921; Richards, 1931)

$$\frac{\partial \theta}{\partial t} - \frac{\partial}{\partial z} \left[K \left(\frac{\partial h}{\partial z} - 1 \right) \right] = 0, \tag{1}$$

where θ is the volumetric water content (cm³/cm³). t is time (s). z is the vertical axis (positive downward, cm). h is the water pressure head (cm). K is the unsaturated hydraulic conductivity (cm/s), which is parameterized as a function of water content θ (Mualem, 1976; van Genuchten, 1980).

The transport of a PFAS may be described by the advection-dispersion equation coupled with two-domain non-equilibrium models for the adsorption at solid–water and air–water interfaces (e.g., Brusseau 2020; Guo et al., 2020),

$$\frac{\partial(\theta C)}{\partial t} + \rho_b \frac{\partial(C_{s,1} + C_{s,2})}{\partial t} + \frac{\partial(C_{aw,1} + C_{aw,2})}{\partial t} + \frac{\partial(\theta vC)}{\partial z} - \frac{\partial}{\partial z} \left(\theta D \frac{\partial C}{\partial z}\right) = 0, \tag{2}$$

$$\frac{\partial c_{s,2}}{\partial t} = \alpha_s [(1 - F_s) K_f C^N - C_{s,2}] \text{ and } C_{s,1} = F_s K_f C^N,$$
 (3)

$$\frac{\partial c_{aw,2}}{\partial t} = \alpha_{aw} \left[(1 - F_{aw}) A_{aw} K_{aw} C - C_{aw,2} \right]$$
and $C_{aw,1} = F_{aw} A_{aw} K_{aw} C.$ (4)

In Eqs. (2–4), C is the aqueous concentration of PFAS (μ mol/cm³). ρ_b is soil bulk density (g/cm²). $v = q/\theta$ is the interstitial porewater velocity (cm/s), where $q = -K(\partial h/\partial z - 1)$ is the Darcy flux. $D = \alpha_L v + \tau D_0$ is the dispersion coefficient (cm²/s), where α_L is the longitudinal dispersivity (cm). τ is the tortuosity factor for the water phase (–) and can be approximated as $\tau = \theta^{7/3}/\theta_s^2$ (Millington and Quirk, 1961) where θ_s is the saturated water content (–), and D_0 is the molecular diffusion coefficient in free water (cm²/s). $C_{s,1}$ and $C_{s,2}$ are SPA concentrations in the "instantaneous" and "kinetic" sorption domains (μ mol/g). Similarly, $C_{aw,1}$ and $C_{aw,2}$ are AWIA concentrations where the sorption is "instantaneous" and limited by diffusive mass transfer (μ mol/cm³), respectively. F_s and $F_{aw} \in [0,1]$ are the fractions of sorbent and air—water interfaces where sorptions are instantaneous (–). α_s and α_{aw} are, respectively, the first-order rate constant for kinetic SPA and AWIA (s⁻¹). K_f (μ mol/g)/(μ mol/cm³) and N (–) are coefficients for the Freundlich isotherm for SPA as suggested by prior experiments (e.g., Wei et al., 2017; Brusseau et al., 2019a; Brusseau, 2020). A_{aw} is the air—water interfacial area (cm²/cm³), which is parameterized as an empirical function of water saturation S_w by fitting air—water interfacial area data measured by aqueous interfacial tracer tests (Brusseau et al., 2007; Brusseau et al., 2015; Araujo et al., 2015). K_{aw} is the AWIA coefficient (cm³/cm²), which can be computed based on the Gibbs equation as $K_{aw} = \Gamma/C$, where the

surface excess $\Gamma = -\frac{1}{\chi RT} \left(\frac{\partial \sigma}{\partial \ln C}\right)_T$ (e.g., Rosen and Kunjappu, 2012). σ (dyn/cm) is the surface tension; χ equals to 1 for nonionic PFAS or ionic PFAS in solutions with swamping electrolyte, and equals to 2 for ionic surfactants in solutions with no swamping electrolyte (such as DIW); R = 8.314 (J/K/mol) is the universal gas constant; T(K) is temperature.

152

153

154

155

156

157

158

159

160

161

162

163

164

165

166

167

168

169

170

171

172

173

174

175

At PFAS-contaminated sites, variably saturated flow (Eq. (1)) and PFAS transport (Eqs. (2-4)) are fully coupled—water flow drives advection and dispersion of PFAS, while changes of PFAS concentration in the aqueous phase, in turn, modify surface tension and capillary forces. The SIF is represented by scaling the capillary pressure (or water pressure head) as $h = \frac{\sigma}{\sigma_0} \cdot \frac{\cos \gamma}{\cos \gamma_0} h_0$ (Bear, 1972; Leverett, 1941), where γ is the contact angle, h_0 and γ_0 indicate the water pressure head and contact angle in PFAS-free solution. Surface tension as a function of PFAS concentration can be modeled by the Szyszkowski equation $\sigma =$ $\sigma_0[1 - b \ln(1 + C/a)]$ (e.g., Adamson & Gast, 1997; Chang & Franses, 1995; Rosen & Kunjappu, 2012), where σ_0 (dyn/cm) is the surface tension at C=0, and a (μ mol/cm³) and b (–) are parameters obtained via fitting to measured surface tension data. Because the present work focuses on anionic PFAS that have a relatively minor impact on the contact angle, we assume $\frac{\cos \gamma}{\cos \gamma_0} \approx 1$ and $h = \frac{\sigma}{\sigma_0} h_0$. We note that for cationic, zwitterionic, or nonionic PFAS that can interact more strongly with soil grain surfaces, the change of contact angle can be more significant and may need to be accounted for especially at higher aqueous concentrations. While contact angle measurements for non-PFAS surfactants exist in the literature (e.g., Desai et al., 1992; Karagunduz et al., 2001), no such data have yet been reported for PFAS that allows parameterization in mathematical models. h₀ is parameterized as a function of water content using the soil-water characteristic function proposed by van Genuchten (1980).

The four unknowns in Eqs. (1–4), h, C, $C_{s,2}$, and $C_{aw,2}$, are solved simultaneously using a fully implicit Newton-Raphson iteration solver. Detailed information for the spatial and temporal discretization, iteration schemes, as well as the treatment of initial and boundary conditions, is presented in Guo et al. (2020).

2.2 Model validation

We employ three measured transport datasets reported in the literature to validate the mathematical model presented in Section 2.1. Based on the conditions examined in these laboratory miscible-displacement experiments, we focus on validating the following processes: (1) SIF (Karagunduz et al., 2015), (2) solution chemistry (Li et al., 2021), and (3) different PFAS input concentrations (Lyu et al., 2018; Brusseau, 2020).

2.2.1 SIF

Karagunduz et al. (2015) conducted a set of miscible-displacement experiments to study the impact of SIF on water flow and the transport of Triton X-100, a non-PFAS surfactant. The Triton X-100 solution was injected under steady-state conditions into five columns packed with unsaturated F70 Ottawa sand. The input concentration ($C_0 = 1,054 \text{ mg/L}$) was much higher than the critical micelle concentration (CMC = 150 mg/L). Five different input water fluxes—corresponding to five initial water contents were used, resulting in different water outflow fluxes and breakthrough curves (BTCs) for the surfactant and a non-reactive solute (NRS), all of which were measured in the experiments. The original simulations reported in Karagunduz et al. (2015) accounted for SIF and equilibrium solid-phase adsorption, but adsorption at the air—water interfaces was not represented. It was reported that the simulations deviated from the measured experiment data at lower water saturations when AWIA becomes more important. Here, we account for a set of comprehensive processes in the simulations including SIF and rate-limited and nonlinear SPA and nonlinear AWIA. AWIA was assumed to be effectively instantaneous because kinetics were determined to be of minor importance.

We employ the independently determined soil hydraulic parameters and solid-phase adsorption isotherm from Karagunduz et al. (2015), and surface tension data from Janczuk et al. (1995) to parameterize the model. The measured surface tension σ as a function of the aqueous concentration C of the surfactant is fitted using the Szyszkowski model (Figure S1 of Supporting Information (SI)). Note that σ and K_{aw} become approximately constant when the aqueous concentration exceeds the CMC. We also account for

the impact of kinetic SPA; the kinetic SPA parameters are obtained by calibrating the model simulation to Exp1 that has the highest water saturation for which AWIA would be least relevant. The obtained kinetic SPA parameters are then used for simulating the other four experiments. Because A_{aw} as a function of water saturation S_w was not measured for the F70 Ottawa sand, we approximate $A_{aw}(S_w)$ using the dataset from a similar sand (i.e., Accusand) that is well-characterized in the literature (e.g., Guo et al., 2020; Brusseau et al., 2019b). The detailed input parameters for the model simulations are summarized in Table S1 in SI.

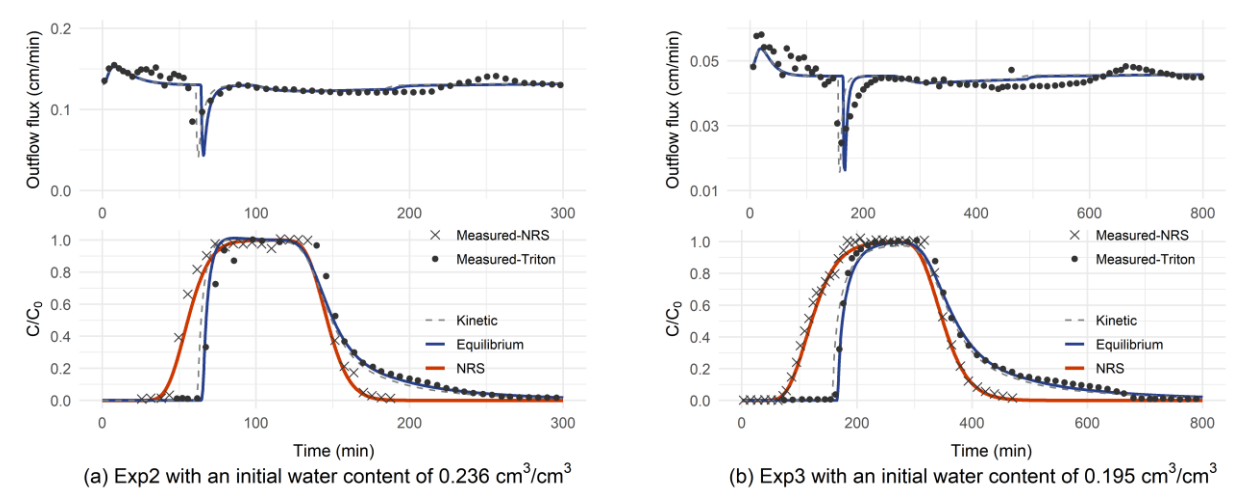


Figure 1. Comparisons between the predicted and measured outflow water flux and BTCs for the miscible-displacement experiments for the high-concentration Triton-X100 in water-unsaturated sand-packed columns. Results presented in (a) and (b) are for soil columns #2 and #3 (i.e., Exp2 and Exp3) in the original experiments. The results for the other experiments can be found in Figure S4 *in SI*.

Very good agreement is observed between the model predictions and the experimental measurements. We observe that a ratio ranging from 0.5 to 1.0 is needed to scale A_{aw} for the model predictions to match the measured BTCs, and the required scaling ratio decreases for smaller water saturations. This appears to indicate that the amount of accessible air—water interfaces may depend on water saturation. Additionally, the results show that kinetic SPA has a limited impact on improving the match between the simulated and measured outflow water flux and the surfactant breakthrough curves. Comparisons for two of the experiments (i.e., Exp2 and Exp3) are presented in Figure 1 as examples. The comparisons for the other three experiments and additional information for the experiments and numerical simulations are provided in Section S1.1 of SI.

The measured perturbations in the water outflow flux caused by the SIF are well captured by the simulations (Figure 1). The outflow flux first increases due to enhanced drainage when the surfactant is applied. Later on, the outflow flux abruptly decreases when the surfactant arrives at the outlet, and then recovers as the surfactant solution reaches a steady state. These behaviors are consistent with the original analysis by Karagunduz et al. (2015). Finally, outflow water flux experiences a further perturbation when the surfactant solution is replaced by clean water. Comparison between the BTCs for the surfactants and NRS shows that the surfactant experiences significant retention resulting from adsorption at solid–water and air–water interfaces, both of which appear to be well captured by the model simulations. Overall, the good agreement between the simulations and measurements demonstrates that the mathematical model of Guo et al (2020) is capable of representing the impact of SIF on variably saturated flow and surfactant transport.

2.2.2 Solution chemistry

To validate our model for representing the impact of solution chemistry on PFAS transport, we simulate the transport experiments by Li et al. (2021) that employed different solution chemistries. In these experiments, 4.6 pore volumes of PFOA solution at 1 mL/min and 6.8 μ g/L were injected into an unsaturated sand column (Accusand, $S_w = 0.64$). After that, the injection was switched to a background electrolyte solution. An NRS was also employed and measured for comparison. The experiments employed six background electrolyte solutions, comprising three different ionic strengths, i.e., 1.5, 10, and 30 mM, and two salts, i.e., NaCl and CaCl₂, to examine the impact of ionic strength and cation valency. Mathematical modeling of these experiments was not reported in the original work.

We simulate the experiments using both equilibrium and kinetic adsorption models. Basic properties including column dimensions, bulk density, porosity, and water saturation were reported in the source paper. K_d was determined from experiments reported for saturated-flow conditions. Soil hydraulic properties and the A_{aw} as a function of S_w are obtained from measured data reported by Brusseau and colleagues for Accusand. Because the sand used here is Accusand, parameters for kinetic SPA and kinetic AWIA

determined for PFOA in Accusand from Lyu et al. (2018) and Brusseau (2020) are employed for the kinetic simulations (see Section 2.2.3). All parameters used for modeling are determined independently. Our simulations suggest that the simulated BTCs are sensitive to the longitudinal dispersivity α_L . $\alpha_L = 0.35$ cm determined from the inverse modeling of the BTC for an NRS under the same unsaturated condition is employed in the simulations presented in Figure 2. More simulated BTCs as influenced by different α_L are presented in Figure S5 of SI. Additional details for the parameters and model setup are given in Section S1.2 of SI.

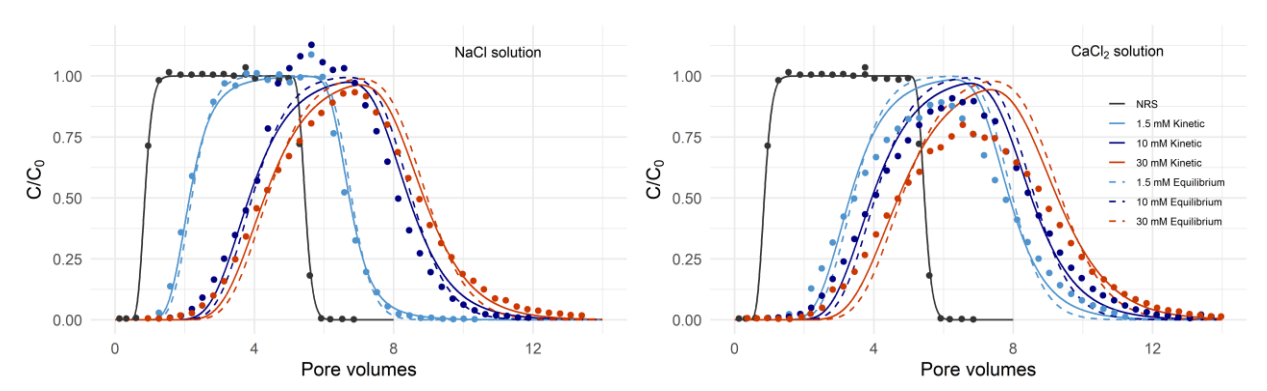


Figure 2. Comparisons between the predicted and measured BTCs for the miscible-displacement experiments for PFOA in water-unsaturated sand-packed columns under different solution chemistry conditions (NaCl vs. CaCl₂). Dots with different colors indicate data measured in different solution chemistry. The corresponding solid lines are simulation results with kinetic SPA and kinetic AWIA models, while the dash lines are the results for which equilibrium adsorption models are applied.

Comparisons between the predicted and measured BTCs show that the model simulations with and without accounting for kinetic SPA and kinetic AWIA are close to each other (Figure 2) indicating that the kinetics associated with SPA and AWIA are insignificant under the specific conditions employed in these experiments. We note that because SPA is much smaller than AWIA (see the fractional retardation factors in Table S2 in the SI), the (relatively small) difference between the equilibrium and kinetic simulations is mainly caused by kinetic AWIA. Comparisons among the BTCs corresponding to different solution chemistry also show that stronger ionic strength leads to stronger retention, which is well captured by the numerical simulations. Similarly, because SPA is very small, the increased retention of PFAS observed at stronger ionic strengths is mainly a result of greater AWIA.

2.2.3 Different PFAS input concentrations

We simulate the experimental data reported in Lyu et al. (2018) and Brusseau (2020) to validate our model for simulating PFAS transport under different input concentrations to test the impact of potential nonlinear adsorption and transient flow caused by SIF. The original simulations presented in Brusseau (2020) assumed steady-state flow and did not account for SIF. The simulations here account for variably saturated flow and potential SIF in the presence of PFAS in the solution. The experiments were conducted at three different input concentration for PFOA ($C_0 = 0.01 \text{ mg/L}$, 0.1 mg/L, and 0.00 mg/L) and four different water saturations ($S_w = 1$, 0.00 mg/L), 0.00 mg/L, and 0.00 mg/L). The data for an NRS is used to obtain the longitudinal dispersivity. All parameters used in the simulations were determined independently. Thus, the model simulations represent direct predictions of the experiments. The list of parameters used and the setup of the numerical model are provided in Section S1.3 of SI.

Comparisons between the model predictions and the experimental data are presented in Figure 3 which show very good agreement for all of the five breakthrough curves covering PFOA input concentrations from 0.01 to 1 mg/L. The results for the NRS are presented for reference. Simulations assuming equilibrium SPA and AWIA are also presented. The results suggest that kinetic SPA and kinetic AWIA have a relatively small impact on the simulated BTCs for all of the PFOA experiments, and the kinetics were mainly caused by kinetic SPA with a minimal contribution from kinetic AWIA (i.e., turning off kinetic AWIA has a minimal impact on the simulated BTCs). We note that because the elution tailing data for the presented experiments were not measured, the kinetic adsorption was only evaluated based on tailing for the arrival front. More rigorous evaluation of the kinetic adsorption will require the elution tailing data. Additionally, simulations accounting for SIF and nonlinear AWIA and SPA are very similar to those without including SIF and assumed linear AWIA and SPA (results not shown), which indicates that the influence of SIF and nonlinearity in adsorption are both minimal for the range of concentrations examined in the experiments. These results are consistent with the simulation results presented in Brusseau et al. (2021) for PFOA, PFOS, and GenX transport in unsaturated sand.

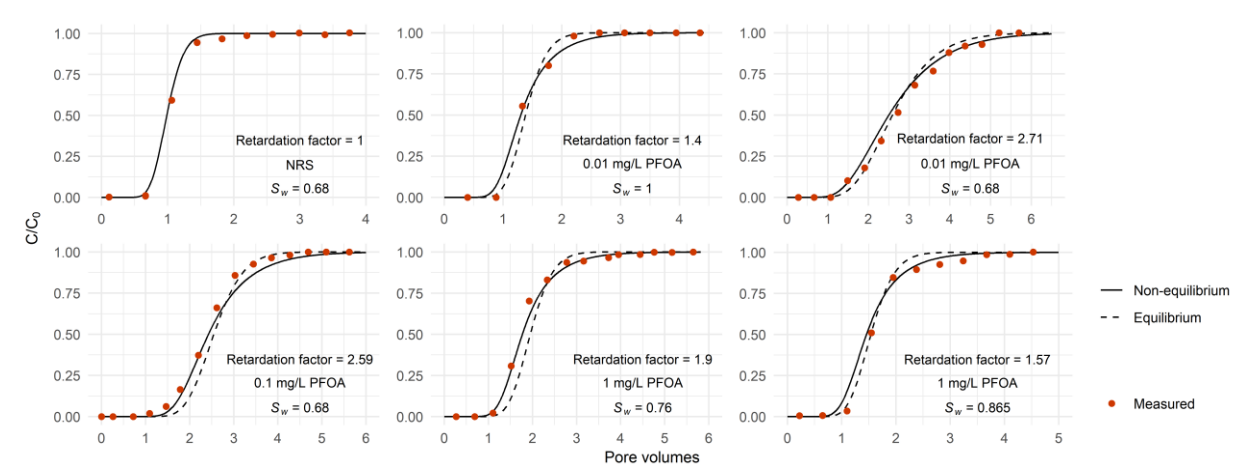


Figure 3. Comparisons between the predicted and measured BTCs for the miscible-displacement experiments for PFOA in sand-packed columns under different input concentrations. Red dots are measured data. Dash lines indicate simulation results for which equilibrium SPA and AWIA models are applied, and solid lines are the results with kinetic SPA and AWIA models. A pore volume is equal to the water volume in the sand column.

Overall, the detailed comparisons between model simulations and measured datasets presented in Sections 2.2.1–2.2.3 for miscible-displacement experiments conducted under a wide range of conditions represent a comprehensive validation of the PFAS-specific flow and transport processes incorporated in the mathematical model introduced in Section 2.1. Additionally, the results suggest that while kinetic SPA and kinetic AWIA may influence the transport of surfactants and PFAS, their impact is of relatively small significance under the specific conditions employed in the above-discussed miscible-displacement experiments. This is consistent with the prior studies by Brusseau (2020) and Brusseau et al. (2021). The significance of the kinetics associated with SPA and AWIA under vadose-zone-relevant conditions will be quantified and discussed in Section 3.1.3.

In the next section, we employ the validated model to conduct detailed simulations at a model FTA site to delineate the primary factors that control the long-term retention and leaching of PFAS in the vadose zone under field-relevant conditions.

2.3 Simulating the long-term leaching and retention of PFAS at an FTA site

2.3.1 General description of the model FTA site

To focus on examining the complex physical and chemical processes for PFAS transport, we assume that the vadose zone of the model FTA site is homogeneous and is composed of one of the two soil media that have different hydraulic and geochemical properties: Accusand (natural quartz sand) or Vinton soil (sandy loam). We use long-term rainfall and evapotranspiration data measured at two sites in Arizona (AZ) and New Jersey (NJ) to represent a semi-arid climate and a humid climate, respectively. This gives a combination of four sets of conditions (two soil media combined with two climatic conditions) for the base simulations.

We assume that regular fire training operations lasted for 30 years at the site (Moody and Field, 2000, 1999), after which no PFAS were released to the site (i.e., post-contamination). The vadose zone is assumed to be PFAS-free before the site was converted for fire training. Based on a report by the Federal Aviation Administration (FAA, 2010) and the information for the volume of AFFF solutions used at FTA sites (Dauchy et al., 2019; Moody and Field, 1999, 2000), we estimate that 50 to 150 gallons (189.3 to 567.8 L) of diluted AFFF solution is applied to a burning area of 385 m² to 1,318 m² per training session (Guo et al., 2020). Assuming that all of the released AFFF solutions enter the vadose zone, this leads to a total infiltration of approximately 0.0458 cm AFFF solution per training session. Fire training activities are assumed to occur every 10 days with each training session lasting for 30 minutes, which are consistent with the standard fire training practices reported in the literature (e.g., Rotander et al., 2015; APEX, 2017; Moody & Field, 1999, 2000).

2.3.2 Data and parameters

(1) PFAS properties

PFAS composition in commercial AFFF formulations varies by year of production and manufacturer (Houtz et al., 2013; Place and Field, 2012). For illustrative purposes, we consider six PFAS including three perfluoroalkyl sulfonic acids (PFSAs) (i.e., PFBS, PFHxS, and PFOS) and three perfluoroalkyl carboxylic

acids (PFCAs) (i.e., PFPeA, PFOA, and PFTrDA). PFBS and PFPeA are short-chain and the remaining four are long-chain based on the terminology proposed by Buck et al. (2011). In our study, chain length refers specifically to the fluorinated-carbon chain length. These six PFAS are among the representative fluorocarbon components of a commercial AFFF concentrate. In this 1:100 diluted AFFF product, the concentrations (C_0) for PFBS, PFPeA, PFHxS, PFOA, PFOS, and PFTrDA are 1.4, 0.23, 7.1, 0.9, 100, and 0.00012 mg/L, respectively (Høisæter et al., 2019), which will be employed in our simulations. The molecular weight (M_w), molar volume (V_m), Szyszkowski fitting parameters for surface tension (a and b), Freundlich parameters for solid-phase adsorption (K_f and N), and molecular diffusivity (D_0) for the six PFAS are presented in Table 1.

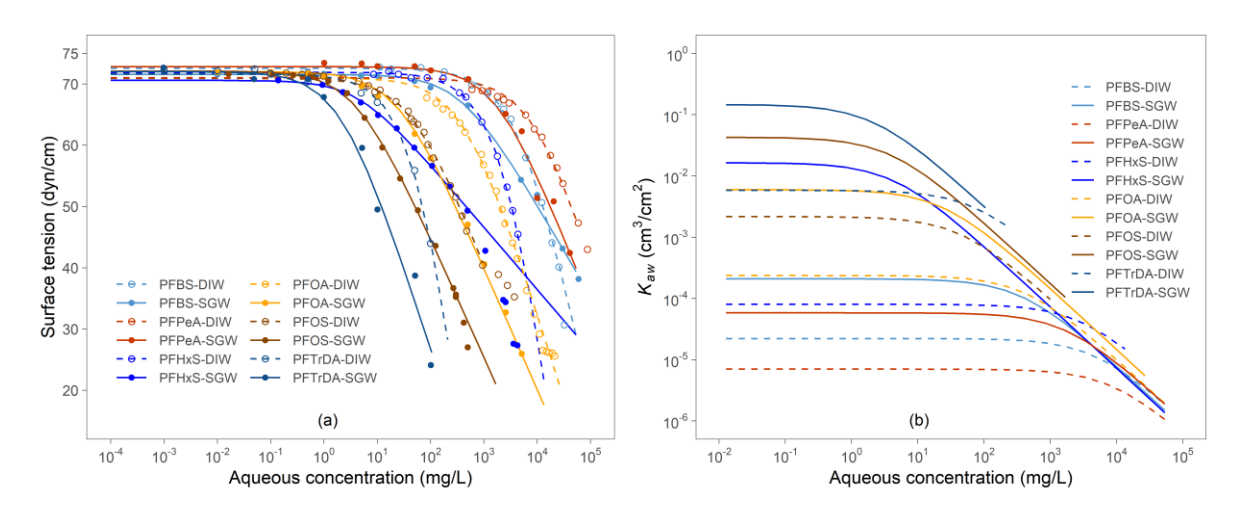


Figure 4. Parameters for the interfacial activities of the six PFAS used in the simulations: (a) surface tension and (b) K_{aw} as a function of PFAS aqueous concentration. The dots in plot (a) are measured data obtained from the literature and the lines are fitted curves to the Szyszkowski equation. Data sources: (1) PFBS-DIW and PFHxS-DIW (Campbell et al., 2009); (2) PFOS-DIW (Costanza et al., 2019); (3) PFBS-SGW, PFHxS-SGW, and PFOS-SGW (Van Glubt et al., 2021), PFPeA-DIW and PFOA-DIW (Tamaki et al., 1989), PFPeA-SGW, PFOA-SGW, PFTrDA-DIW, and PFTrDA-SGW (Brusseau & Van Glubt, 2019).

The surface tension data measured in DIW and SGW (Brusseau and Van Glubt, 2019; Campbell et al., 2009; Costanza et al., 2019) are plotted in Figure 4(a). Specifically, the data for PFPeA-SGW, PFOA-SGW, PFTrDA-SGW, and PFOS-SGW are from Brusseau & Van Glubt (2019), PFBS-DIW and PFHxS-DIW are from Campbell et al. (2009), and PFOS-DIW are from Costanza et al. (2019). The SGW employed in Brusseau and Van Glubt (2019) included Na⁺ (50 mg/L), Ca²⁺ (36 mg/L), Mg²⁺ (25 mg/L), NO₃⁻ (6 mg/L), Cl⁻ (60 mg/L), CO₃²⁻/HCO₃⁻ (133 mg/L), and SO₄²⁻ (99 mg/L). The pH and ionic strength were 7.7 and 0.01

M, respectively. The AWI adsorption coefficient for each compound, K_{av} , is computed based on the surface tension data and the Gibbs adsorption equation (Figure 4(b)). The molecular diffusivities (D_0) for all compounds, except for PFTrDA, are measured values from Schaefer et al. (2019b). Do for PFTrDA is estimated by relating it to the molar volume using the regression $\ln D_0 = -2.5623 \ln V_m + 1.5528$ (Schaefer et al., 2019b). The Freundlich SPA parameters K_f and N for PFOS in Accusand and Vinton soil and PFOA in Accusand were reported in prior studies (Van Glubt et al., 2021; Brusseau, 2020; Guo et al., 2020). For other PFAS, because no measured SPA isotherms are available for the two porous media, we estimate K_f and N as follows. We assume that the nonlinear coefficient N for PFBS and PFHxS is the same as that for PFOS in the same medium, that is, N is 0.81 for Accusand and 0.77 for Vinton soil. Similarly, we assume N for PFPeA and PFTrDA in both media is the same as that for PFOA in Accusand, i.e., N = 0.87. We employ this simple estimation for N partly because the nonlinearity for solid-phase adsorption was reported to be weak for a wide range of sediments (Guelfo & Higgins, 2013; Higgins & Luthy, 2006) and also specifically for the two media we use (Brusseau et al., 2019; Brusseau, 2020). For K_f , we estimate the values for the other two PFSAs by scaling the K_f for PFOS based on the PFSA organic carbon-normalized distribution coefficients (K_{oc}) reported in the literature (Brusseau, 2019b; Higgins and Luthy, 2006). The K_f for PFOA in the Vinton soil is estimated by scaling K_f for PFOA in the Accusand based on the K_f values for PFOS in the two media. Similar to the PFSAs, the K_f for the other two PFCAs are then estimated by scaling K_f for PFOA based on the reported PFCA K_{oc} values (Brusseau, 2019b; Guelfo and Higgins, 2013). The molar volumes (V_m) are obtained from the PubChem database (URL: pubchem.ncbi.nlm.nih.gov).

334

335

336

337

338

339

340

341

342

343

344

345

346

347

348

349

350

351

352

353

354

355

356

357

Parameters for kinetic SPA and kinetic AWIA are only available for PFOA. We estimate the first-order rate constants for the other PFAS from that of PFOA assuming that the first-order rate constants scale with the molecular diffusion coefficients, for example, $\alpha_s^{\text{PFPeA}}/\alpha_s^{\text{PFOA}} = D_0^{\text{PFPeA}}/D_0^{\text{PFOA}}$ and $\alpha_{aw}^{\text{PFPeA}}/\alpha_{aw}^{\text{PFOA}} = D_0^{\text{PFPeA}}/D_0^{\text{PFOA}}$ (e.g., Brusseau, 2020). The estimated α_s and α_{aw} are presented in Table 1.

Table 1. Parameters for the six PFAS.

Name	PFBS	PFPeA	PFHxS	PFOA	PFOS	PFTrDA
M_w (g/mol)	300.1	264.05	400.12	414.07	500.13	664.11
$V_m^{[1]}$ (cm ³ /mol)	165.7	154.2	217.3	237.3	271.8	369
Solution chemistry	DIW SGW	DIW SGW	DIW SGW	DIW SGW	DIW SGW	DIW SGW
σ_0 (dyn/cm)	72.55 71.55	71 72	71.89 70.59	71 72	70.91 72.08	71.61 72.01

<i>a</i> (μmol/cm ³) <i>b</i> (–)		16.4 1.28 0.243 0.091	35.9 6.82 0.172 0.132	7.68 0.011 0.416 0.063	1.07 0.0597 0.172 0.12	0.0933 0.0082 0.138 0.118	0.118 0.0034 0.464 0.164
$\frac{b(-)}{K_{oc}(\text{cm}^3/\text{g})}$		25.7	23.4	91.2	104.7	616.6	17,839.5
K_f ^[2]	Accusand	1.920×10 ⁻³	1.023×10 ⁻²	6.812×10 ⁻³	4.569×10 ⁻²	4.605×10 ⁻²	7.783
	Vinton	1.108×10^{-2}	5.903×10 ⁻²	3.931×10 ⁻²	2.637×10^{-1}	2.658×10^{-1}	44.92
N [2]	Accusand	0.81	0.87	0.81	0.87	0.81	0.87
1 V 1	Vinton	0.77	0.87	0.77	0.87	0.77	0.87
$D_0 (10^{-}$	⁻⁶ cm ² /s) [3]	11	12	4.5	4.9	5.4	1.25
F_s	$(-)^{[4]}$	$0.4^{[5]}$	$0.4^{[5]}$	$0.4^{[5]}$	0.4	0.4	0.4
α_s (1)	/hour) [4]	13.24 [5]	14.45 [5]	5.42 [5]	5.90	6.50	1.51
F_{aw}	· (-) ^[4]	0.9	0.9	0.9	0.9	0.9	0.9
α_{aw} (1/hour) [4]		11.00	12.00	4.50	4.90	5.40	1.25

Note: [1] The molar volumes (V_m) are obtained from URL: pubchem.ncbi.nlm.nih.gov. [2] The units are (µmol/g)/(µmol/cm3)^N for K_f and (–) for N. K_f for PFTrDA is obtained using the QSPR method (Brusseau & Van Glubt, 2019). [3] D_0 are measured by Schaefer et al. (2019b) except for PFTrDA. For PFTrDA, D_0 is estimated by the regression $\ln D_0 = -2.5623 \ln V_m + 1.5528$ (Schaefer et al., 2019b). [4] The F_s and F_{aw} are determined from measurements for PFOA (miscible-displacement experiments in Section 2.2.3) and are estimated for the other five PFAS. [5] We also consider the kinetics of SPA for these three PFAS from PFAS-contaminated soils collected from a historically AFFF-impacted site (Schaefer et al., 2021). For PFBS, PFPeA, PFHxS, $\alpha_s = 1.2 \times 10^{-3}$, 1.1×10^{-3} , and 2×10^{-4} (1/hour), while $F_s = 0.25$, 0.67, and 0.41, respectively.

To estimate the uncertainty associated with the measured surface tension data, we collect 11 data sets for PFOA in DIW from the literature (An et al., 1996; Chen et al., 2005; Downes et al., 1995; Dmowski, 1990; López-Fontán et al., 2005; Lunkenheimer et al., 2015; Lunkenheimer et al., 2017; Lyu et al., 2018; Shinoda et al., 1972; Tamaki et al., 1989; Vecitis et al., 2008). The original data and the fitted curves are presented in Figure S8(a). The Szyszkowski equation is fitted separately to each of the datasets. Note that the curve using the parameters averaged from the separately fitted parameters agrees well that fitted with all measured data (see a comparison in Figure S9). The computed K_{aw} as a function of C is presented in Figure S8(b). The variations in these measured data may be caused by differences in the forms of PFOA (e.g., acid vs. different salt forms) and the employed experimental conditions (e.g., temperature, the status of instruments, or expertise of an operator).

There is a wide range of uncertainty in the fitted parameters for PFOA as shown in Figure S8. Specifically, σ_0 ranges from 70.0 to 73.75 dyn/cm, with a mean value of 71.45 dyn/cm, and a coefficient of variation CV = 0.0146. a ranges from 0.945 to 3.145 (μ mol/cm³), with a mean value of 1.884 (μ mol/cm³), and CV = 0.382. b (–) ranges from 0.187 to 0.312, with a mean value of 0.231, and CV of 0.185. The resulting maximum K_{aw} in Figure S8(b) ranges from 0.13×10⁻³ to 0.29×10⁻³ cm³/cm², with a mean value of 0.196×10⁻³ cm³/cm², and CV = 0.27. In our study, CV = σ/μ , where σ is the standard deviation. The CVs

and correlation coefficients obtained for PFOA (see Table 2) are then used to represent the uncertainties associated with the surface tension parameters for all PFAS. We assume that σ_0 , a, and b follow normal distributions based on the datasets we use though more measured data would be needed to further confirm this assumption.

Table 2. Coefficient of variation (CV) and correlation coefficients for the randomized PFAS parameters that will be used for the parameter uncertainty analyses.

Donomoton	CV		Correlation coefficients	
Parameter	CV	σ_0	а	b
σ_0	0.0153	1	_	_
а	0.382	0.3051	1	_
b	0.194	0.5206	0.9014	1

Two porous media (Accusand and Vinton soil) are used as the base media in the present work. The

Accusand is a commercially available natural quartz sand (UNIMIN Corp.), which has a median grain

(2) Soil properties

diameter of 0.35 mm. It has a total organic carbon content of 0.04%, The Fe, Mn, and Al oxide contents are 14, 2.5, and 12 µg/g, respectively. The Vinton soil is a loamy sand collected locally in Tucson, Arizona. The hydraulic properties, solid-phase adsorption behavior, and measured air—water interfacial area as a function of water saturation for the two media, are reported in Guo et al. (2020) and the references therein. Here we summarize the soil parameters in Table 3. α (cm⁻¹) and n (–) are the parameters in the van Genuchten-Mualem empirical model (Mualem, 1976; van Genuchten, 1980). The air—water interfacial area A_{avv} was measured by aqueous interfacial tracer experiments, which was shown to represent the total hydraulically accessible air—water interfacial area consisting of capillary interfaces associated with menisci between bulk air and water, and film-associated interfaces associated with wetting films surrounding grain surfaces. Additionally, the A_{avv} data used in our study also agrees well with several other AWI data sets measured using low concentrations of surfactant tracers wherein SIF was negligible by design (Brusseau et al., 2020). The measured A_{avv} was fitted to a second-degree polynomial function of water saturation S_{vv} , $A_{avv} = x_2S_{vv}^2 + x_1S_{vv} + x_0$, where x_2 , x_1 , and x_0 are the fitting parameters (–). For Accusand, $x_2 = 548.54$, $x_1 = -1,182.5$, and $x_0 = 633.96$, while for Vinton soil, $x_2 = 1,305.0$, $x_1 = -2,848.6$, and $x_0 = 1,543.6$ (Guo et al., 2020). α_L is the longitudinal dispersivity (cm) that is approximated using the empirical function $\alpha_L = 1,182.5$ and $\alpha_L = 1,182.5$ and $\alpha_L = 1,182.5$ are the longitudinal dispersivity (cm) that is approximated using the empirical function $\alpha_L = 1,182.5$

83(log(L/100))^{2.414} (Xu and Eckstein, 1995), where L (cm) is the apparent length scale which is set to the depth of the vadose zone. In our study, L = 400 cm. We note that the approximation employed here assumes saturated condition and hence does not account for the impact of water saturation on α_L .

Table 3. Parameters for Accusand and Vinton soil.

Soil type	K_s (cm/s)	$\theta_s (\text{cm}^3/\text{cm}^3)$	$\theta_r (\text{cm}^3/\text{cm}^3)$	ρ_b (g/cm ³)	α (cm ⁻¹)	n (-)	α _L (cm)
Accusand	2.1×10 ⁻³	0.294	0.015	1.650	0.04477	4	24.38
Vinton soil	1.17×10^{-3}	0.395	0.056	1.627	0.02178	3.451	24.38

We use the Vinton soil as the base porous medium and perturb its parameters for the sensitivity and uncertainty simulations. In Table 4, we provide the uncertainty of soil parameters described by CV and correlation coefficient that will be used for the parameter uncertainty analyses later. We assume that these soil parameters follow normal or log-normal distributions. The CVs for the soil hydraulic parameters, $\ln K_s$, θ_s , θ_r , $\ln \alpha$, and n, were obtained from field measurements (Russo & Bouton, 1992). The correlation coefficients for the majority of these parameters are measured from undisturbed soils at the field site (Russo & Bouton, 1992) except for the ones related to θ_r for which no measured values were available and were thus estimated using the Rosetta-3 pedotransfer function model (Zhang & Schaap, 2017). The CVs for K_f and N are obtained from parameters measured by Van Glubt et al. (2021). K_f and N are assumed to be independent. The range of uncertainty for $\ln \alpha_L$ is estimated based on a statistical study (Xu & Eckstein, 1995). The bulk density ρ_b exhibits a narrow range from field measurement (Russo & Bouton, 1992) and is thus assumed a constant.

Table 4. Coefficient of variation (CV) and correlation coefficients for the randomized soil parameters.

D	CV	D-f	Correlation coefficients ^[1]				
Parameters	CV	References	$\log K_s$	θ_s	θ_r	log α	n
$\log K_s$	0.26		1	-	_	_	_
θ_s	0.056	Field measurement for undisturbed soils	0.657	1	-	_	_
$ heta_r$	0.056	(Russo & Bouton, 1992)	-0.01	-0.087	1	_	_
$\log \alpha$	0.264	(Russo & Bouton, 1992)	0.293	0.255	-0.266	1	_
n	0.067		-0.205	-0.085	0.280	-0.279	1
Kf	0.12	Laboratory measurement					
N	0.05	(Van Glubt et al., 2021)	_		_		
$log \alpha_L$	0.3	Estimated from Xu & Eckstein (1995)	_				

Note: [1] Correlation coefficients related to θ_r were predicted separately from the Vinton soil using the Rosetta-3 model (Zhang & Schapp, 2017) because no field-measured data are available. The soil texture for the Vinton soil used in this study is 96% sand, 1.5% silt, 3% clay (Brusseau et al., 2019a). Other correlation coefficients are obtained from Russo & Bouton (1992). We note that for the Vinton soil with varying texture, these correlation coefficients predicted using the Rosetta-3 Pedotransfer Function model (Zhang & Schaap, 2017) span a wide range.

(3) Precipitation and evapotranspiration

We consider two climatic conditions (semiarid (AZ) vs. humid (NJ)) to examine the impact of climate on the long-term retention and leaching of PFAS in the vadose zone. The semiarid climate is represented by the Walnut Gulch Kendall Grasslands site (Scott, 2004) in Arizona, USA, while the humid climate is represented by the Silas Little site (Clark, 2004) in New Jersey, USA. Precipitation and evapotranspiration data for the two sites for 10 years (01/01/2005-12/31/2014) at a 30-min temporal resolution is downloaded from the AmeriFlux database (URL:https://ameriflux.lbl.gov). The data are repeated every 10 years to generate multidecadal data sets. The 10-year annual average precipitation is 293 mm and 1,066 mm for the two sites, respectively. Note that our model does not account for transpiration through plants; the measured evapotranspiration data were used as the potential evapotranspiration to determine the surface evaporation rate. The original data at a 30-min resolution are smoothed to a 24-hour resolution and employed for the long-term simulations.

2.3.3 Design of numerical experiments

In this section, we introduce the overall design of the numerical experiments which include (1) a set of base simulations that focus on examining the relative importance of several retention and transport processes, and (2) a series of additional simulations that focus on analyzing the sensitivity and uncertainty of parameters that control the long-term leaching and retention of PFAS in the vadose zone. The specific methods employed for conducting the parameter sensitivity and uncertainty analyses are also introduced.

(1) Overview

We first conduct a set of numerical experiments that employ the default parameters and conditions described in Section 2.3.2. These base cases consider two soil media (Accusand vs. Vinton), two climatic conditions (AZ vs. NJ), and six PFAS (PFBS, PFPeA, PFHxS, PFOA, PFOS, and PFTrDA). We then conduct additional simulations to probe the influence of different parameters and conditions on transport. The additional simulations allow us (1) to analyze the impact of several factors (i.e., soil porewater solution chemistry & chain length, nonlinear adsorption, and kinetic adsorption) on the long-term retention and leaching of PFAS in the vadose zone; (2) to identify the primary parameters that control the predicted

leaching behavior by performing sensitivity analysis for 12 parameters used in the simulations; and (3) to conduct Monte Carlo simulations to analyze the uncertainties in the model predictions propagated from the uncertainty in the input parameters.

(2) Estimating the air—water interfacial area (A_{aw}) for a random soil

Perturbations on soil parameters may introduce significant variations in A_{aw} . The A_{aw} of a random soil may be related to the soil-water characteristic curve based on the thermodynamic approach (Bradford & Leij, 1997; Bradford et al., 2015; Morrow, 1970; Leverett, 1941),

$$A_{aw}^{thermo}(\theta) = \frac{1}{\sigma_0} \int_{\theta}^{\theta_S} p_c \, d\theta, \tag{5}$$

where p_c is the capillary pressure parameterized as a function of θ . $p_c = -\rho_w gh$, where ρ_w is the density of water (g/cm³), g is the gravitational constant (cm/s²). For the van Genuchten model (van Genuchten, 1980), $p_c = \frac{\rho_w g}{\alpha} (S_e^{-1/m} - 1)^{1/n}$ (g·cm/s²), where S_e is the effective water saturation (–). Substituting $S_e = \frac{(\theta - \theta_r)}{(\theta_s - \theta_r)}$ to Eq. (5) yields

$$A_{aw}^{thermo}(S_e) = \frac{(\theta_s - \theta_r)\rho_w g}{\sigma_0 \alpha} \int_{S_e}^{1} \left(S_e^{-1/m} - 1\right)^{1/n} dS_e.$$
 (6)

However, the thermodynamic-based A_{aw}^{thermo} was reported to significantly underestimate the tracer-based A_{aw}^{tracer} (Jiang et al., 2020), which has been considered to be more transport-relevant (Lyu et al., 2018; Brusseau et al., 2019b; Brusseau and Guo, 2021). Assuming that the ratio between the thermodynamic-based A_{aw}^{thermo} and the tracer-based A_{aw}^{tracer} remains the same for all soils, we estimate the tracer-based A_{aw}^{tracer} for a random soil based on the thermodynamic-based A_{aw}^{thermo} and measured tracer-based A_{aw}^{tracer} from the Vinton soil. That is,

$$A_{aw,random}^{estimated}(S_e) = \omega(S_e) \cdot A_{aw,random}^{thermo}(S_e), \tag{7}$$

where $\omega(S_e) = A_{aw,Vinton}^{tracer}(S_e)/A_{aw,Vinton}^{thermo}(S_e)$ is the scaling ratio computed from the tracer-based $A_{aw,Vinton}^{tracer}(S_e)$ and the thermodynamic-based $A_{aw,Vinton}^{thermo}(S_e)$ for the Vinton soil. The integral in Eq. (6) can be evaluated by numerical integration. Because the variation of ω is relatively small for different S_e , we approximate it using the ratio $\omega = 4.2$ evaluated at $S_e = 0.5$ for our simulations.

(3) Morris sensitivity analysis

We employ the Morris method (Morris, 1991) for the parameter sensitivity analysis. The Morris method quantifies the global sensitivity using local derivatives of the model predictions in the parameter space, i.e., only a single parameter is perturbed at a time. In our sensitivity analysis, we use the arrival time to the bottom of the domain to represent the speed of predicted PFAS migration. We define the arrival time (t_a) for each PFAS as the time when 0.1% of the total mass of this PFAS has exited the bottom boundary of the domain.

Suppose η_i is the perturbed parameter. $\eta_i \in [\mu_i(1 - CV_i), \ \mu_i(1 + CV_i)]$ where μ_i denotes the mean of η_i (i.e., the original measured mean value) and CV_i is the estimated coefficient of variation for parameter η_i . We define the normalized parameter as $P_i = \eta_i/\mu_i$. Furthermore, we denote $t_{a,i}$ and $t_{a,0}$ as the arrival times for the simulations with the perturbed parameter and the base case, respectively, and define the normalized arrival time as $S_i = t_{a,i}/t_{a,0}$. Then, the local sensitivity, measured as Elementary Effects (EE_i), has the following form

$$EE_i = \frac{\partial S_i}{\partial P_i} = \frac{S(\eta_i) - S(\mu_i)}{P(\eta_i) - P(\mu_i)}.$$
 (8)

The mean value of EE_i for all of the m perturbations performed to η_i is then defined as the Morris sensitivity $M_i = \frac{1}{m} \sum_{k=1}^{m} |EE_i^k|$ for η_i , where k = 1, 2, ..., m is the index for different simulated perturbations.

For our problem specifically, we denote the parameter space by $\eta_i = \sigma_0$, a, b, $\log K_s$, θ_s , θ_r , $\log \alpha$, n, $\log \alpha_L$, K_f , and N, where i = 1, 2, ..., 11. Additionally, the boundary-condition parameter ($\log C_0$) is used to quantify the sensitivity of model predictions to the applied concentration. Based on laboratory measurements and field investigations (see Section 2.3.2), the parameters are all assumed to follow normal distributions. Note that this means K_s , α , and α_L follow log-normal distributions. The mean value μ_i is the reference value measured or estimated for the original soil or PFAS. We conduct the sensitivity analysis for each PFAS, which gives a total of 6 sets of simulations. In each set of simulations, we conduct simulations by uniformly changing each of the 12 parameters within the designated range. When one of the parameters is being perturbed, the remaining parameters are fixed to their mean values. The applied PFAS

concentration ranging from $0.1C_0$ to $10C_0$ is used to investigate the model predictions as influenced by the applied concentration. The above perturbations are conducted for the prediction of long-term leaching for all six PFAS using the base case of Vinton soil under NJ climate.

(4) Monte Carlo simulations

We employ Monte Carlo simulations to quantify the uncertainties in model predictions propagated from the uncertainties in the model parameters. 200 combinations of randomized parameters for Vinton soil and the six PFAS are generated (see Section 2.3.2). Specifically, the randomly perturbed surfacial properties of 200 PFAS based on the measured parameters for PFBS, PFPeA, PFHxS, PFOA, PFOS, and PFTrDA in SGW are presented in Figure S10 of SI. These parameters, i.e., σ_0 , a, and b, follow normal distributions. Their mean values, CV, and correlation coefficients are provided in Table 2. The corresponding randomly generated K_{aw} as a function of aqueous concentration is presented in Figure S11 of SI. The 200 realizations of the randomly generated soil parameters are presented in Figure S12 of SI. These parameters, i.e., $\log K_s$, θ_s , θ_r , $\log \alpha$, n, A_{aw} , K_f , N, and $\log \alpha_L$, follow normal distributions and have mean values, CV, and correlation coefficients reported in Table 4.

It is important to note that not all of the 12 parameters are independent. Several of them are correlated and their correlation is taken into account in our sensitivity and uncertainty analyses. (1) The Szyskowski parameters (σ_0 , a, and b) are correlated based on measured data for PFOA in DIW (see Table 2). (2) The soil hydraulic parameters are correlated based on field measurement for 417 undisturbed soil samples (Russo & Bouton, 1992) (see Table 4). (3) A_{aw} is related to soil hydraulic properties using the thermodynamic-based method discussed in subsection (2) above (Bradford & Leij, 1997; Bradford et al., 2015; Morrow, 1970; Leverett, 1941). Finally, the parameters for kinetic SPA and AWIA are kept as constants in the simulations for sensitivity and uncertainty analyses because the impact of kinetic adsorption on the predicted long-term PFAS is relatively minor (see Section 3.1.3).

2.3.4 Setup of the numerical model

We consider a 1D domain along the vertical dimension of a 4-m deep vadose zone. The 1D domain is discretized using a uniform grid ($\Delta z = 2$ cm). For the Newton-Raphson iterative solver, all of the following absolute tolerances have to be met for convergence at each time step: $\delta h = 1 \times 10^{-3}$ cm, $\delta \theta = 1 \times 10^{-4}$ cm³/cm³, and $\delta C = 1 \times 10^{-7}$ μ mol/cm³. The initial conditions are set as h(z, t = 0) = -100 cm and C(z, t = 0) = 0. The top boundary is represented by measured rainfall infiltration and surface evaporation. During the fire-training sessions, an inward PFAS solution lasting 30 minutes enters the top numerical cell; the infiltration rate and applied PFAS concentrations (C_0) for each PFAS are provided in Section 2.3.1. A zero-gradient condition is assigned for both water flow ($\partial h/\partial z|_{z=4}$ m = 0) and PFAS transport ($\partial C/\partial z|_{z=4}$ m = 0) at the bottom boundary of the domain.

3 Results and discussion

The results and analyses are organized as follows. We first examine the impact of several primary factors including solution chemistry, PFAS chain length, and nonlinear SPA and AWIA on the long-term retention and leaching of PFAS in the vadose zone based on the set of base simulations. Then, we present detailed analyses on the impact of parameter sensitivity and uncertainty on long-term model predictions based on the Morris sensitivity and Monte Carlo simulations.

3.1 Primary factors

3.1.1 The impact of solution chemistry & chain length

We conduct simulations using surface tension parameters for the six PFAS determined in solutions with different ionic strengths (DIW vs. SGW) to quantify the impact of solution chemistry and chain length on long-term retention and leaching of PFAS in the vadose zone. Note that while the ionic strengths vary among simulations, they do not dynamically change over time in each simulation.

Figure 5 presents the simulated spatial concentration profiles over time for six PFAS under two different ionic strengths (DIW vs. SGW). The Vinton soil & NJ climate scenario is shown as an example.

The results show that PFAS retention in the vadose zone increases with both ionic strength and chain length. Comparing the simulated retention using DIW vs. SGW surface activities, significantly enhanced retention is observed for PFHxS, PFOA, and PFOS. For instance, the t_a (arrival time) for PFHxS increases from 2.5 years for DIW to 15 years for SGW. Similarly, the t_a for PFOA increases from 8 years for DIW to 19 years for SGW. The t_a for PFOS for DIW is 12 years, while PFOS reached the bottom of the domain 64 years later for SGW. It is noted that employing DIW as the representative low ionic-strength solution does not reflect natural soil conditions and is used to illustrate extreme differences. The range of ionic strengths relevant for soil porewater will typically be less disparate, and therefore the impact on PFAS retention will be of lesser significance (e.g., Brusseau and Van Glubt, 2019; Lyu & Brusseau, 2020; Silva et al., 2019).

Conversely, a relatively minor increase is observed in Figure 5 for the retention of PFBS, PFPeA, and PFTrDA in SGW. This is because the significance of SPA is comparable to or greater than AWIA for these three PFAS. For example, at a simulated representative aqueous concentration for PFTrDA in the vadose zone (6×10⁻⁷ mg/L), the SPA is 10 times greater than the AWIA such that the retention of PFTrDA is completely dominated by SPA. We note that prior batch and miscible-displacement experiments have shown that SPA can also increase with ionic strength (Li et al., 2021; Lyu & Brusseau 2020). Our simulations have not accounted for the impact of ionic strength on the SPA due to a lack of data for the PFAS and soil media considered in the present study.

At the same ionic strength, the retention follows the same order of chain length as PFBS < PFHxS < PFOS, and PFPeA < PFOA < PFTrDA. The disparity in the speed of migration for PFAS with different chain lengths is consistent with concentration depth profiles reported at many AFFF-impacted FTA sites (Baduel et al., 2017; Brusseau et al., 2020a; Casson & Chiang, 2018; Dauchy et al., 2019). Specifically, the cited field studies showed that long-chain PFAS were typically the dominant compounds near the surface in the vadose zone, while short-chain PFAS represented the majority of PFAS mass at deeper depths. The concentrations of long-chain PFAS in the soil were consistently the highest near the surface of the vadose zone and decreased exponentially along depth, albeit the sites were contaminated by different sources at various periods. Conversely, the short-chain PFAS were much more uniformly distributed along depth and

had reached much deeper locations. More quantitatively, the maximum concentrations of PFOS in our simulations (on the order of $10^4 \,\mu\text{g/kg}$) are within the range of those reported at the AFFF-impacted FTA sites ($10^3 \sim 10^5 \,\mu\text{g/kg}$) (Baduel et al., 2017; Brusseau et al., 2020a; Casson and Chiang, 2018; Dauchy et al., 2019). One of the few studies that reported measured PFTrDA is that of Dauchy et al. (2019), who measured PFAS soil concentrations for an AFFF-impacted site that had been used as an FTA for more than 30 years. They observed that PFTrDA was only detected above the depth of 0.25 m, indicating much stronger retention of PFTrDA in the vadose zone compared to PFOA and PFOS. This is in agreement with our simulated results where PFTrDA remains above the depth of 0.5 m even 50 years after the PFAS-release contamination events have ceased. The direct implication of the above analysis is that, unlike short-chain PFAS, leaching of long-chain PFAS from the vadose zone to groundwater will likely persist for several decades or longer after the PFAS-release events have been stopped.

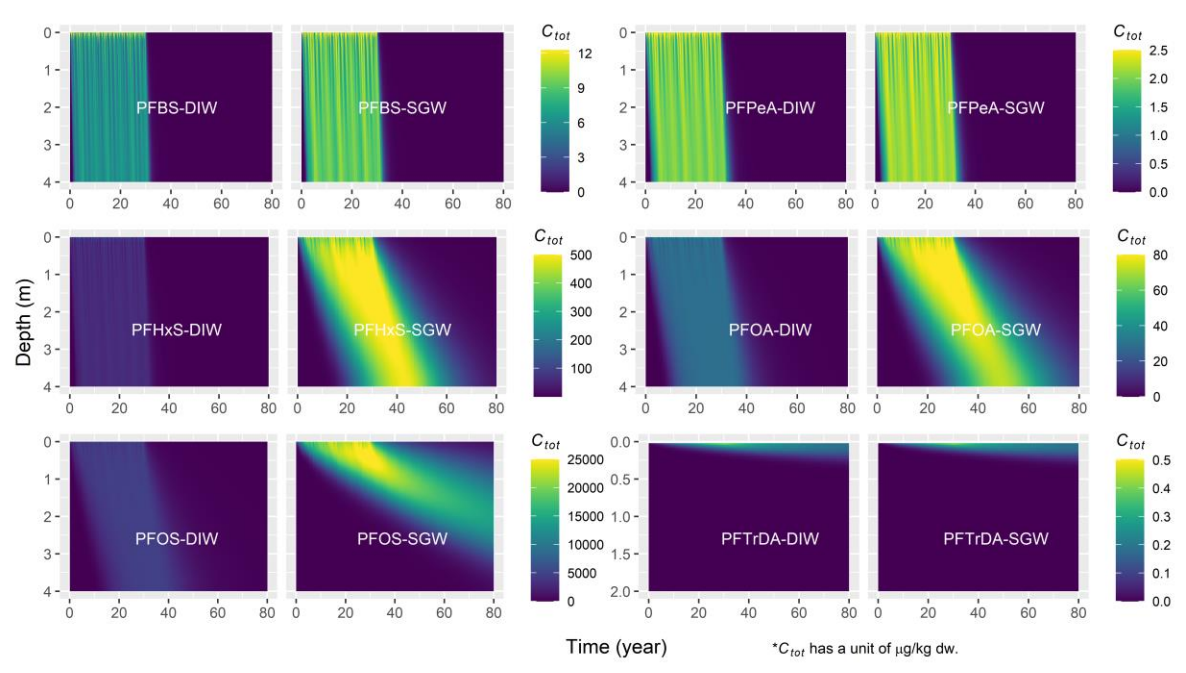


Figure 5. Simulated spatial concentration profiles over time for six PFAS released to the vadose zone. Simulations using the surface tension parameters measured in DIW and SGW are presented for comparison. The results are from the cases using Vinton soil & NJ climate. All simulations include a 30-year active-contamination period and a 50-year post-contamination period. C_{tot} is the total concentration of the PFAS (μ g/kg dw), which includes the mass of PFAS in the aqueous phase, and at the soil–water and air–water interfaces. For better visualization, the upper limit of the simulated C_{tot} for PFBS, PFPeA, PFHxS, PFOA, and PFOS are trimmed to 12, 2.5, 500, 80, 25,000 μ g/kg dw, respectively.

3.1.2 The impact of nonlinear adsorption

To examine the impact of nonlinearity in SPA and AWIA on long-term PFAS retention in the vadose zone, we conduct additional simulations assuming linear SPA and AWIA and compare the results with the full-process model where nonlinear SPA and AWIA are accounted for. For linear SPA and AWIA, K_d and K_{aw} for a PFAS need to be computed at a given aqueous concentration. For our simulations, we computed K_d and K_{aw} at $C = C_{max}/2$, where C_{max} is the simulated maximum aqueous concentration from the full-process model. For the example scenario of Vinton soil & NJ climate, the maximal concentrations for PFBS, PFPeA, PFHxS, PFOA, PFOS, and PFTrDA are $C_{max} = 0.12$ mg/L, 0.019 mg/L, 0.29 mg/L, 0.032 mg/L, 0.09 mg/L, and 0.34 ng/L, respectively. To isolate the impact of nonlinear SPA and AWIA, we construct simulation cases involving three levels of nonlinearity: (1) nonlinear SPA and AWIA ("full model"), (2) linear AWIA but nonlinear SPA ("constant K_{aw} "), and (3) linear SPA and linear AWIA ("constant K_d & K_{aw} ").

The results show that nonlinear SPA has a notable impact on the retention of some of the PFAS (Figure 6). This is because PFAS concentrations vary greatly within the plume and over time, which leads to relatively strong variations in the equivalent K_d . For example, within the majority of the plume (where $C > 0.1\%C_{max}$), the equivalent $K_d = K_f C^{N-1}$ varies from 0.07 to 0.33 cm³/g for PFBS and from 0.22 to 1.1 cm³/g for PFPeA during the simulation. However, the impact of nonlinear SPA varies among the PFAS—it has a stronger impact on the retention of PFBS, PFPeA, and PFTrDA than on that of PFHxS, PFOA, and PFOS because SPA is comparable with or greater than AWIA for the former. Conversely, nonlinearity in AWIA has a minimal impact for all PFAS except for PFOS. Close inspection reveals that the aqueous concentrations for PFBS, PFPeA, PFHxS, PFOA, and PFTrDA are all very low so that the corresponding K_{avv} approaches the maximum K_{avv} . The K_{avv} at $C = C_{max}/2$ are 2.08×10^{-4} , 5.78×10^{-5} , 5.90×10^{-3} , 5.93×10^{-3} , and 0.146 cm³/cm² and the maximum K_{avv} are 2.08×10^{-4} , 5.78×10^{-5} , 5.94×10^{-3} , 5.93×10^{-3} , and 0.146 cm³/cm² for these five PFAS. The aqueous concentration of PFOS is much higher than the other PFAS and the nonlinearity leads to a greater variation in K_{avv} —the simulated K_{avv} varies from 0.043 to 0.022 cm³/cm²

in the full model, which is not represented adequately by the model with linear AWIA (i.e., constant K_{aw}). A log-scale version of Figure 6 is presented in Figure S6 of the SI to better visualize the differences between the model simulations at lower concentrations.

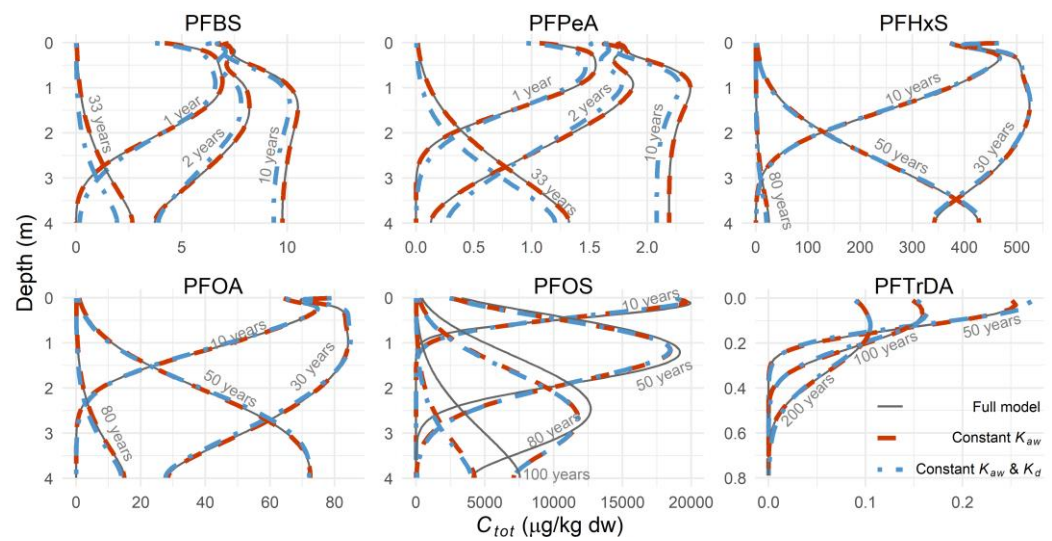


Figure 6. Simulated spatial concentration profiles over time for six PFAS obtained using models with different levels of nonlinearity in the adsorption terms. In the legend, "Full model" indicates fully nonlinear SPA and AWIA (solid thin grey line), "constant K_{aw} " indicates nonlinear SPA only (solid thick red line), and "constant K_{aw} & K_d " indicates linear SPA and AWIA (dashed blue line). All simulations include a 30-year active-contamination period and a 50-year post-contamination period. C_{tot} is the total concentration of the PFAS (μ g/kg dw), which includes the mass of PFAS in the aqueous phase, and at the soil–water and air–water interfaces.

The above analyses predicted that the impact of nonlinearity of adsorption on PFAS leaching is concentration-dependent. To further examine the dependence of nonlinear SPA and AWIA on concentration, we conduct additional simulations for PFOS at a wide range of applied concentrations including $0.001C_0$, $0.01C_0$, $0.1C_0$, $0.1C_0$, $0.1C_0$, and $0.01C_0$. The results suggest that the retention decreases as the applied concentration increases. The time for the peak concentration of the plume to reach a depth of 1 m is approximately 64, 60, 56, 43, 22, and 14 years for the increasing applied concentrations $(0.001C_0, 0.01C_0, 0.1C_0, 0$

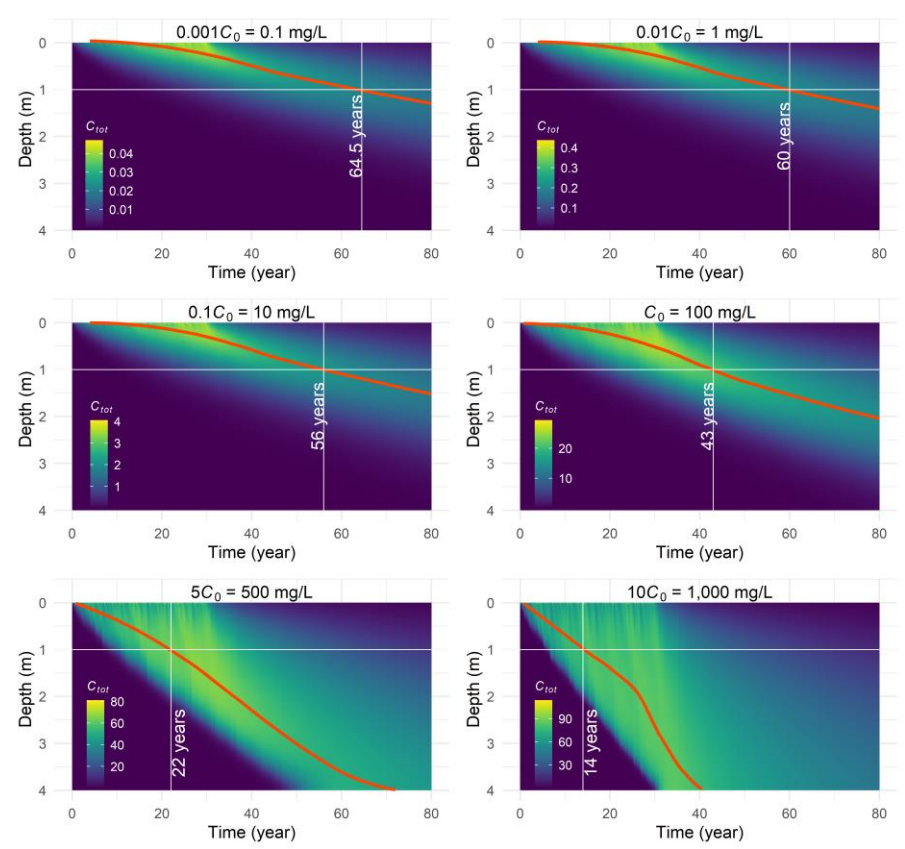


Figure 7. Simulated spatial concentration profiles over time for PFOS applied at concentrations from 0.001 to 10 times to that of the original concentration, i.e., 0.1 mg/L, 1 mg/L, 10 mg/L, 100 mg/L, 500 mg/L, and 1,000 mg/L. Red solid lines are the recorded trajectories of the peak concentration. The time when the peak concentration plume reaches a depth of 1 m is labeled by the vertical white solid line and is reported in the text. C_{tot} is the total concentration (μ g/kg dw), which includes the mass of PFAS in the aqueous phase, and at the soil–water and air–water interfaces

Our simulations suggest that the nonlinearity in the AWIA is minor for all of the PFAS except for PFOS that is applied at a much greater concentration than the others. This is consistent with the findings reported by Brusseau et al (2021) where nonlinearity in AWIA was estimated to be insignificant at concentrations sufficiently lower than the critical reference concentration (defined as the concentration corresponding to a reduction of 2.5% in the surface tension). For the simulations presented in the present study that are relevant to field conditions, even though the applied concentrations can be quite high (e.g., 100 mg/L for PFOS), the aqueous concentrations of PFAS decrease significantly (well below 3.8 mg/L) after entering the vadose zone due to strong adsorption at the solid—water and especially air—water interfaces. This implies that the actual porewater concentrations in the vadose zone, rather than the applied concentrations of PFAS, need to be used when evaluating the importance of the nonlinearity of AWIA at

the field sites. When nonlinearity in AWIA is insignificant, the AWIA isotherm can be simplified by using a constant K_{aw} and there is no need to employ the Szyszkowski and Gibbs equations to compute the concentration-dependent K_{aw} in the model.

Finally, we note that the issue of whether air—water interfacial adsorption follows the Langmuir isotherm and becomes linear at low concentrations is still under debate (Schaefer et al., 2019a; Arshadi et al., 2020; Schaefer et al., 2020). Additional data and analyses reported recently indicated that K_{aw} approaches a constant at relatively high concentrations and remains constant at concentrations down to 1 μ g/L for PFOA (Brusseau et al., 2021) and approximately 5×10^{-6} M for two hydrocarbon surfactants SDBS and SDS (Brusseau, 2021).

3.1.3 The impact of kinetic adsorption

We examine the impact of kinetic adsorption by comparing the simulation results with or without accounting for kinetic SPA and kinetic AWIA. The parameters for kinetic adsorption are obtained from the miscible-displacement experiments in Section 2.2.2 (Table 1) and from batch experiments conducted on PFAS-contaminated soils collected from a historically AFFF-impacted site (Schaefer et al., 2021; the parameters are reported in Note [5] of Table 1). The latter was suggested to have more pronounced kinetics in SPA especially for the shorter-chain PFAS in the soils collected from the shallow vadose zone (Schaefer et al., 2021). Two soils and two climatic conditions are considered for all six PFAS in the simulations. Note that the results of the batch experiments reported in Schaefer et al. (2021) suggested that kinetic SPA is much stronger for the short-chain than that for the long-chain PFAS, we thus only employ the measured kinetic SPA parameters for the three shorter-chain PFAS (PFBS, PFPeA, and PFHxS) in our simulations.

The simulated cumulative mass discharge out of the domain with and without accounting for kinetic SPA and kinetic AWIA is presented in Figure 8. Overall, the difference between the simulations with and without accounting for kinetic adsorption is quite small. A log-scale version of Figure 8 is presented in Figure S7 of the SI, but the difference remains small even at much lower values of mass discharge. This is also true for the simulations that employed the kinetic parameters from PFAS-contaminated soils collected

from a historically AFFF-impacted site that exhibit much stronger kinetics in SPA (Schaefer et al., 2021). These simulations suggest that the impact of kinetic SPA and kinetic AWIA on the predicted long-term PFAS leaching is minimal under the field-relevant conditions examined in the present study.

659

660

661

662

663

664

665

666

667

668

669

670

671

672

673

674

675

676

677

678

679

680

681

682

683

A close inspection reveals that the simulated mean porewater velocities in the field-scale simulations are at least one or two orders of magnitude smaller than those employed in the miscible-displacement experiments. In addition, the retardation factor is also generally much greater in the field-scale simulations due to much lower water saturations (and hence stronger AWIA). In our study, we define the Damköhler numbers for kinetic SPA and kinetic AWIA as $Da_s = \alpha_s L/\bar{q}$ and $Da_{aw} = \alpha_{aw} L/\bar{q}$, where \bar{q} is the mean Darcy flux. The fractional retardation factors contributed by SPA and AWIA are $R_s = \rho_b/\theta \cdot \partial C_s/\partial C =$ $N\rho_b K_f C^{N-1}/\theta$ and $R_{aw} = 1/\theta \cdot \partial C_{aw}/\partial C \approx K_{aw} A_{aw}/\theta$. We define the total retardation factor as $R_{tot} = 1/\theta \cdot \partial C_{aw}/\theta$ $1 + R_s + R_{aw}$. The retardation factors and the Damköhler numbers computed for the simulations presented in Figure 8 are summarized in Table 5. For the same kinetic SPA and kinetic AWIA parameters, the Damköhler numbers computed for the field-scale simulations are several orders of magnitude greater than those computed from the miscible-displacement experiments (see Tables S2 and S3). The Da_s computed from the simulations that employed the kinetic SPA parameters determined from the historically AFFFimpacted soil samples are smaller due to the stronger kinetics, but they are still mostly greater than 10 (see Da_s in the parentheses for the three shorter-chain PFAS). While the Da_s for PFHxS can be smaller than 10, the SPA is much less important than AWIA for PFHxS such that the kinetic SPA plays a minor role in influencing the overall leaching.

In contrast, the miscible-displacement experiments have much greater porewater velocity and smaller retardation factors. The Damköhler numbers for those experiments, which are generally much smaller, are reported in Tables S2 and S3 in SI. In addition, AWIA is also less significant due to the much smaller air—water interfacial area at greater water saturations. Taking the experiment with PFOA input at $C_0 = 1$ mg/L and $S_w = 0.76$ as an example (Section 2.2.3), the porewater velocity is 837.5 cm/d (note that the mean value is as low as 0.5-11.3 cm/d under the simulated field conditions) and the fractional retardation factors are

 $R_s = 0.38$ and $R_{aw} = 0.57$. The resulting Damköhler numbers Da_s and Da_{aw} are 9.27 and 7.70, respectively.

Table 5. Damköhler numbers for the long-term simulations [1].

$ \begin{array}{c ccccccccccccccccccccccccccccccccccc$	lable 5. Damkonier numbers for the long-term simulations [1].								
PFBS	PFAS	Soil	Climate	R_{s} (-)	R_{aw} (–)	R_{tot} (–)	$Da_{s} (-)^{[2]}$	Da_{aw} (-)	
PFBS		Accusand	ΑZ	0.5	4.8	6.4		9.78×10^{5}	
PFPeA PEA PFPPeA PFPPeA PFPPA PAccusand PAZ PPPA PFPPA	DEDC		NJ	0.5	3.5	5.1	$2.69 \times 10^{5} (24.4)$	2.24×10^{5}	
PFPeA Accusand	FFDS	Vinton	ΑZ	1.1	2.3	4.4	$2.27 \times 10^6 (205.7)$	1.89×10^{6}	
PFPeA PFPeA Accusand NJ 1.9 1.0 3.8 2.94×10 ⁵ (22.4) 2.44×10 ⁵		VIIItoli	NJ	1.1	1.6	3.7	3.15×10^{5} (28.5)	2.61×10^{5}	
PFPeA Vinton		Acqueend	AZ	2.0	1.3	4.4			
Vinton NJ 3.2 0.6 5.1 2.48×10 ⁶ (188.6) 2.06×10 ⁶ NJ 3.2 0.4 4.6 3.43×10 ⁵ (26.1) 2.85×10 ⁵ Accusand AZ 2.4 138.4 141.8 4.82×10 ⁵ (17.8) 4.00×10 ⁵ NJ 1.6 100.1 102.8 1.10×10 ⁵ (4.1) 9.15×10 ⁴ Vinton AZ 5.9 70.1 77.0 9.29×10 ⁵ (34.3) 7.71×10 ⁵ NJ 4.3 44.8 50.1 1.29×10 ⁵ (4.8) 1.07×10 ⁵ Accusand NJ 8.4 100.6 110.0 1.20×10 ⁵ 9.97×10 ⁴ Vinton AZ 22.8 71.5 95.3 1.01×10 ⁶ 8.40×10 ⁵ NJ 17.6 45.2 63.8 1.40×10 ⁵ 1.16×10 ⁵ Accusand NJ 9.8 659.1 669.9 1.32×10 ⁵ 1.10×10 ⁵ Vinton AZ 23.4 434.9 459.3 1.11×10 ⁶ 9.26×10 ⁵ Vinton NJ 21.5 306.5 329.0 1.54×10 ⁵ 1.28×10 ⁵ Accusand AZ 10331.8 4163.2 14496.1 1.34×10 ⁵ 1.11×10 ⁵ Vinton AZ 22625.3 2288.7 24915.0 2.59×10 ⁵ 2.14×10 ⁵	DEDoA	Accusanu	NJ	1.9	1.0	3.8	2.94×10^{5} (22.4)	2.44×10^{5}	
PFTrDA Accusand NJ 3.2 0.4 4.6 3.43×10³ (26.1) 2.85×10³ Accusand NJ 1.6 100.1 102.8 1.10×10⁵ (17.8) 4.00×10⁵ NJ 1.6 100.1 102.8 1.10×10⁵ (4.1) 9.15×10⁴ Vinton NJ 4.3 44.8 50.1 1.29×10⁵ (4.8) 1.07×10⁵ Accusand NJ 8.4 100.6 110.0 1.20×10⁵ 9.97×10⁴ Vinton NJ 17.6 45.2 63.8 1.40×10⁵ 1.16×10⁵ Vinton NJ 9.8 659.1 669.9 1.32×10⁵ 1.10×10⁵ Vinton NJ 9.8 659.1 669.9 1.32×10⁵ 1.10×10⁵ Vinton NJ 21.5 306.5 329.0 1.54×10⁵ 1.28×10⁵ Accusand NJ 8589.6 3060.3 11650.9 3.07×10⁴ 2.54×10⁵ Vinton NJ 8589.6 3060.3 11650.9 3.07×10⁴ 2.54×10⁵ Vinton AZ 22625.3 2288.7 24915.0 2.59×10⁵ 2.14×10⁵	FFFEA	Vinton	ΑZ	3.5	0.6	5.1		2.06×10^{6}	
PFHxS		VIIItoli	NJ	3.2	0.4	4.6	3.43×10^{5} (26.1)	2.85×10^{5}	
PFHxS		Acqueend	AZ	2.4	138.4	141.8	$4.82 \times 10^5 (17.8)$	4.00×10^{5}	
PFOA AZ 5.9 70.1 77.0 9.29×10° (34.3) 7.71×10° PFOA NJ 4.3 44.8 50.1 1.29×10⁵ (4.8) 1.07×10⁵ Accusand AZ 11.8 139.9 152.7 5.24×10⁵ 4.36×10⁵ Vinton AZ 22.8 71.5 95.3 1.01×10⁶ 8.40×10⁵ NJ 17.6 45.2 63.8 1.40×10⁵ 1.16×10⁵ Accusand AZ 10.7 792.3 804.0 5.78×10⁵ 4.80×10⁵ Vinton AZ 23.4 434.9 459.3 1.11×10⁶ 9.26×10⁵ Vinton AZ 23.4 434.9 459.3 1.11×10⁶ 9.26×10⁵ NJ 21.5 306.5 329.0 1.54×10⁵ 1.28×10⁵ PFTrDA AZ 10331.8 4163.2 14496.1 1.34×10⁵ 1.11×10⁶ Vinton AZ 22625.3 2288.7 24915.0 2.59×10⁵ 2.14×10⁵	DELL	Accusand	NJ	1.6	100.1	102.8	$1.10 \times 10^5 (4.1)$	9.15×10^4	
PFOA Accusand AZ 11.8 139.9 152.7 5.24×10 ⁵ 4.36×10 ⁵	ггихэ	Vinton	ΑZ	5.9	70.1	77.0	9.29×10 ⁵ (34.3)	7.71×10^{5}	
PFOA NJ 8.4 100.6 110.0 1.20×10 ⁵ 9.97×10 ⁴ Vinton AZ 22.8 71.5 95.3 1.01×10 ⁶ 8.40×10 ⁵ NJ 17.6 45.2 63.8 1.40×10 ⁵ 1.16×10 ⁵ Accusand NJ 9.8 659.1 669.9 1.32×10 ⁵ 1.10×10 ⁵ Vinton AZ 23.4 434.9 459.3 1.11×10 ⁶ 9.26×10 ⁵ NJ 21.5 306.5 329.0 1.54×10 ⁵ 1.28×10 ⁵ Accusand AZ 10331.8 4163.2 14496.1 1.34×10 ⁵ 1.11×10 ⁵ Vinton AZ 22625.3 2288.7 24915.0 2.59×10 ⁵ 2.14×10 ⁵			NJ		44.8		1.29×10 ⁵ (4.8)		
PFOA NJ 8.4 100.6 110.0 1.20×10 ³ 9.9/×10 ⁴ Vinton AZ 22.8 71.5 95.3 1.01×10 ⁶ 8.40×10 ⁵ NJ 17.6 45.2 63.8 1.40×10 ⁵ 1.16×10 ⁵ Accusand AZ 10.7 792.3 804.0 5.78×10 ⁵ 4.80×10 ⁵ Vinton AZ 23.4 434.9 459.3 1.11×10 ⁶ 9.26×10 ⁵ NJ 21.5 306.5 329.0 1.54×10 ⁵ 1.28×10 ⁵ Accusand AZ 10331.8 4163.2 14496.1 1.34×10 ⁵ 1.11×10 ⁵ NJ 8589.6 3060.3 11650.9 3.07×10 ⁴ 2.54×10 ⁴ Vinton AZ 22625.3 2288.7 24915.0 2.59×10 ⁵ 2.14×10 ⁵		Accusand	AZ	11.8	139.9	152.7	5.24×10^{5}	4.36×10^{5}	
Vinton AZ 22.8 71.5 95.3 1.01×10° 8.40×10° NJ 17.6 45.2 63.8 1.40×10⁵ 1.16×10⁵ Accusand AZ 10.7 792.3 804.0 5.78×10⁵ 4.80×10⁵ NJ 9.8 659.1 669.9 1.32×10⁵ 1.10×10⁵ Vinton AZ 23.4 434.9 459.3 1.11×10⁶ 9.26×10⁵ NJ 21.5 306.5 329.0 1.54×10⁵ 1.28×10⁵ Accusand AZ 10331.8 4163.2 14496.1 1.34×10⁵ 1.11×10⁶ NJ 8589.6 3060.3 11650.9 3.07×10⁴ 2.54×10⁴ Vinton AZ 22625.3 2288.7 24915.0 2.59×10⁵ 2.14×10⁵	DEOA		NJ	8.4	100.6	110.0	1.20×10^{5}		
PFOS Accusand AZ 10.7 792.3 804.0 5.78×10 ⁵ 4.80×10 ⁵ NJ 9.8 659.1 669.9 1.32×10 ⁵ 1.10×10 ⁵ Vinton AZ 23.4 434.9 459.3 1.11×10 ⁶ 9.26×10 ⁵ NJ 21.5 306.5 329.0 1.54×10 ⁵ 1.28×10 ⁵ Accusand AZ 10331.8 4163.2 14496.1 1.34×10 ⁵ 1.11×10 ⁵ NJ 8589.6 3060.3 11650.9 3.07×10 ⁴ 2.54×10 ⁴ Vinton AZ 22625.3 2288.7 24915.0 2.59×10 ⁵ 2.14×10 ⁵	FFOA	Vinton	ΑZ	22.8	71.5	95.3	1.01×10^{6}	8.40×10^{5}	
$ \begin{array}{c ccccccccccccccccccccccccccccccccccc$		Vinton	NJ	17.6	45.2	63.8	1.40×10^{5}	1.16×10^{5}	
PFOS Vinton AZ 23.4 434.9 459.3 1.11×10 ⁶ 9.26×10 ⁵ NJ 21.5 306.5 329.0 1.54×10 ⁵ 1.28×10 ⁵ PFTrDA Accusand AZ 10331.8 4163.2 14496.1 1.34×10 ⁵ 1.11×10 ⁶ NJ 8589.6 3060.3 11650.9 3.07×10 ⁴ 2.54×10 ⁴ Vinton AZ 22625.3 2288.7 24915.0 2.59×10 ⁵ 2.14×10 ⁵		A a auga m d	ΑZ	10.7	792.3	804.0	5.78×10^{5}	4.80×10^{5}	
Vinton AZ 23.4 434.9 459.3 1.11×10° 9.26×10° NJ 21.5 306.5 329.0 1.54×10⁵ 1.28×10⁵ Accusand AZ 10331.8 4163.2 14496.1 1.34×10⁵ 1.11×10⁵ NJ 8589.6 3060.3 11650.9 3.07×10⁴ 2.54×10⁴ Vinton AZ 22625.3 2288.7 24915.0 2.59×10⁵ 2.14×10⁵	DEOC	Accusand	NJ	9.8	659.1	669.9	1.32×10^{5}	1.10×10^{5}	
$ \begin{array}{c ccccccccccccccccccccccccccccccccccc$	Pros	Vintan	ΑZ	23.4	434.9	459.3	1.11×10 ⁶	9.26×10 ⁵	
PFTrDA $\frac{\text{Accusand}}{\text{Vinton}}$ NJ 8589.6 3060.3 11650.9 3.07×10 ⁴ 2.54×10 ⁴ $\frac{\text{Vinton}}{\text{Vinton}}$ AZ 22625.3 2288.7 24915.0 2.59×10 ⁵ 2.14×10 ⁵		vinton	NJ	21.5	306.5	329.0	1.54×10^{5}	1.28×10^{5}	
PFTrDA $\frac{NJ}{Vinton}$ AZ $\frac{8589.6}{22625.3}$ $\frac{3060.3}{2288.7}$ $\frac{11650.9}{24915.0}$ $\frac{3.07 \times 10^4}{2.59 \times 10^5}$ $\frac{2.54 \times 10^4}{2.14 \times 10^5}$	DETD.A	Accusand	ΑZ	10331.8	4163.2	14496.1	1.34×10 ⁵	1.11×10 ⁵	
Vinton AZ 22625.3 2288.7 24915.0 2.59×10 ³ 2.14×10 ³			NJ	8589.6	3060.3	11650.9	3.07×10^4	2.54×10^{4}	
NJ 18020.9 1510.9 19532.8 3.59×10 ⁴ 2.97×10 ⁴	rriida	Vinton	AZ	22625.3	2288.7	24915.0	2.59×10 ⁵	2.14×10 ⁵	
		vinton	NJ	18020.9	1510.9	19532.8	3.59×10^{4}	2.97×10^{4}	

Note: [1] All retardation factors are calculated using the simulation results within the major portion of the plume (where C > 0.1% C_{max}) and during the period of (t = 0-30 years). [2] Numbers in the parentheses are from the simulations that employed the kinetic parameters for SPA determined from batch experiments using PFAS-contaminated soils from a historic FTA site.

The above analyses imply that it may be reasonable to assume equilibrium adsorption when the focus is on predicting PFAS leaching at long time scales, which would allow for simplifying the governing equations and parameters for the numerical simulations. However, we caution that the analyses presented here are based on the kinetic parameters obtained for a limited number of miscible-displacement experiments conducted in a sand media and field-contaminated soil samples from only one historical AFFF-impacted site. The importance of kinetic adsorption under a wider range of conditions for different kinds of field-contaminated sites and different PFAS needs further investigation.

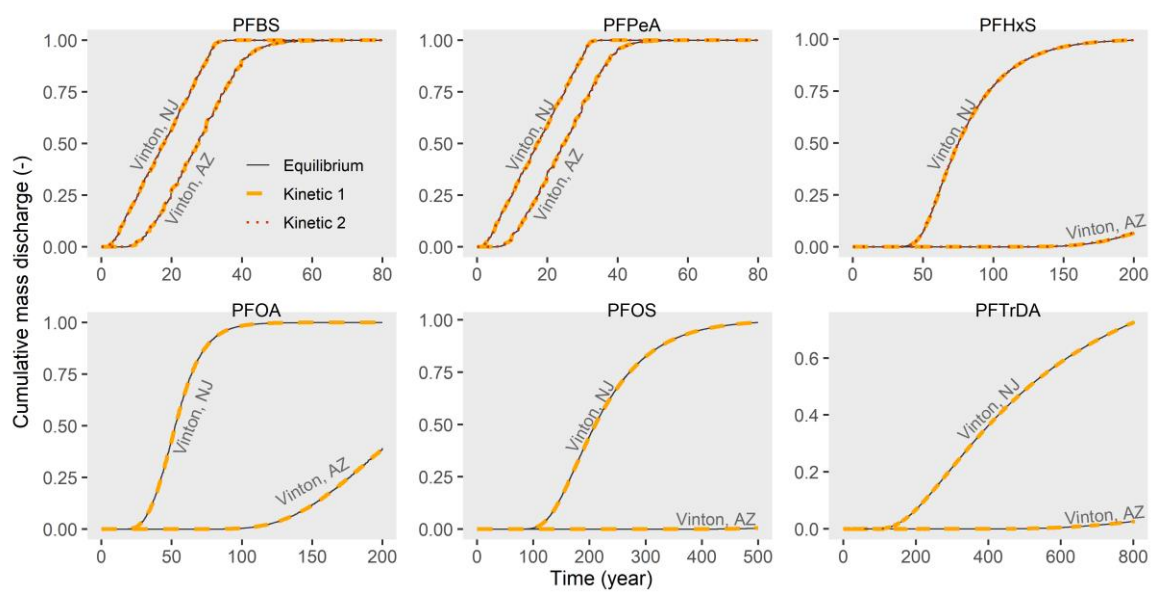


Figure 8. Comparison of cumulative mass discharge simulated using models with equilibrium vs. kinetic adsorption. In the legend, "Kinetic 1" indicates the simulations that employed the kinetic parameters from miscible-displacement experiments in Section 2.2.3 (Lyu et al., 2018; Brusseau, 2020); "Kinetic 2" indicates the simulations that employed the kinetic parameters determined by batch experiments conducted on PFAS-contaminated soil samples collected from a historical AFFF-impacted site (Schaefer et al. 2021). The latter strong kinetic phenomenon was only observed for the three shorter-chain PFAS (i.e., PFBS, PFPeA, and PFHxS). PFTrDA has not arrived at the bottom of the domain in the simulations, thus the cumulative mass discharge at the depth of 100 cm is presented here.

3.2 Parameter sensitivity and uncertainty

3.2.1 Parameter sensitivity analysis

A close inspection reveals that the rank of the most sensitive parameters is controlled by the relative importance of SPA and AWIA, which depends on the chain length and the applied concentration. When SPA is more important (e.g., PFPeA and PFTrDA), the model predictions are most sensitive to changes in the SPA parameters (especially N) due to nonlinear SPA. Conversely, when AWIA is dominant (i.e., for those longer-chain PFAS at relatively greater concentrations, e.g., PFHxS, PFOA, and PFOS), the model predictions are most sensitive to parameters related to $A_{aw}(\log \alpha)$ and interfacial properties (σ_0 , a, and b). For PFBS, SPA and AWIA are comparable (e.g., 30% vs. 43% of mass are partitioned to soil–water and air–water interfaces for the Vinton & NJ scenario), thus the model predictions are sensitive to both the SPA and AWIA. Finally, the model predictions for most of the PFAS are sensitive to dispersivity, which is expected because dispersivity controls the overall spreading of the plume.

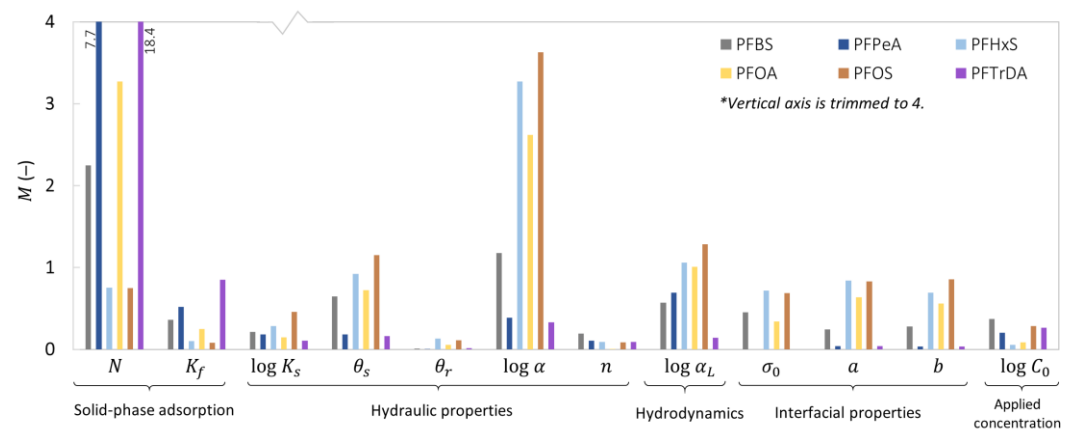


Figure 9. The Morris sensitivity (M) of the normalized arrival time to the normalized parameters for each PFAS. The Morris sensitivity analysis is conducted within the range of one standard deviation for each parameter.

3.2.2 Parameter uncertainty analysis

In this section, 11 of the 12 parameters, i.e., σ_0 , a, b, $\log K_S$, θ_S , θ_r , $\log \alpha$, n, $\log \alpha_L$, K_f , and N are randomly perturbed within the uncertainty ranges provided in Section 2.3.2. For each PFAS, there are 200 realizations based on the case with Vinton soil and under NJ climate.

Figure 10 presents the cumulative mass discharge out of the domain from the Monte Carlo simulations. The results indicate that the leaching rate and the associated range of uncertainty vary strongly among PFAS with different chain lengths. The short-chain PFAS (PFBS and PFPeA) arrive at the bottom of the domain early and the majority of the mass is removed shortly after the contamination was stopped. Even with

randomized parameters, the variation among the different realizations is relatively insignificant. This is because SPA and AWIA are generally weak for the short-chain PFAS and the mass discharge is mainly controlled by hydrologic conditions, such as rainfall intensity. Conversely, the breakthroughs of the long-chain PFAS are much later and the mass discharge can last several decades during the post-contamination period. However, the variation among the realizations is also much greater. The variation is so wide that the realizations for the long-chain PFAS with the fastest leaching are even comparable to those of the short-chain PFAS. For example, the majority of the mass is removed 1–2 years after the PFAS application has ceased for the PFOS realizations with the most rapid leaching; for PFTrDA, it is ~170 years. We note that these fastest leaching cases are well beyond the 95% confidence interval (CI). The arrival times within the 95% CIs are reported in the following paragraph.

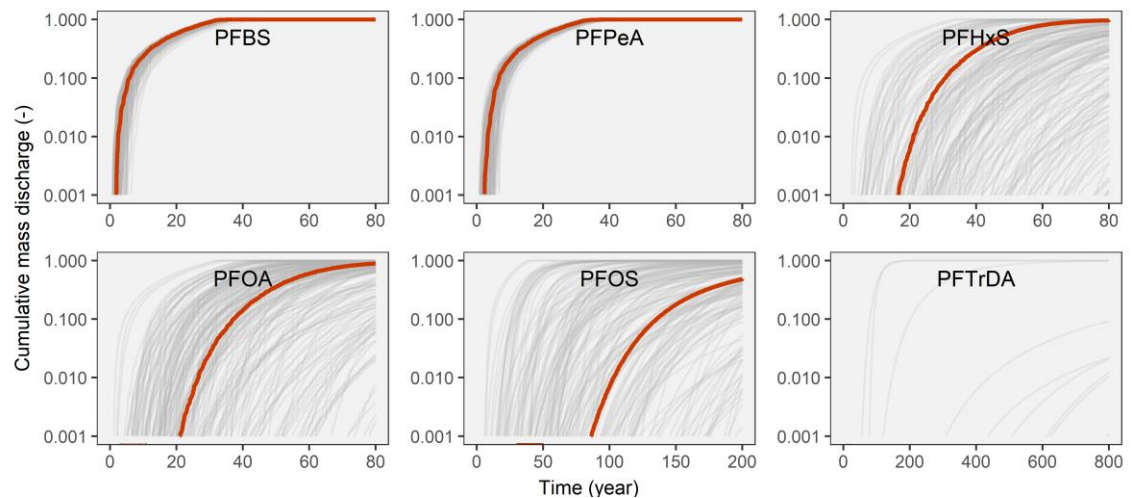


Figure 10. Simulated cumulative mass discharge for each PFAS compared between the random realizations employing the stated ranges of input values (thin grey lines) and the base case using the measured parameters (thick red lines). In the random realizations, there are 11 parameters randomly perturbed within the designated uncertainty ranges, namely, σ_0 , a, b, $\log K_s$, θ_s , θ_r , $\log \alpha_l$, K_l , and N. Due to much slower leaching rates, longer periods were simulated for PFOS and PFTrDA (200 and 800 years, respectively). Note that simulated the base case for PFTrDA has not arrived during the simulation, thus the red solid line is not shown.

Another way to examine the uncertainty in the model predictions is to analyze the statistical distribution of the arrival time (t_a) among the Monte Carlo realizations, which are shown in Figure 11. The computed arrival times for the base cases are also presented, i.e., 1.7 years, 2.4 years, 12 years, 17 years, 63 years, and 1,783 years for PFBS, PFPeA, PFHxS, PFOA, PFOS, and PFTrDA, respectively. Interestingly,

 t_a among the Monte Carlo realizations appear to follow log-normal distributions for all PFAS. The range of uncertainties among the PFAS with different chain lengths are consistent with those observed in Figure 10, i.e., the uncertainty range is much greater for longer-chain PFAS. For example, the 95% CI of t_a is 497–14,571 years for PFTrDA, 10–414 years for PFOS, 5–87 years for PFOA, and 6–112 years for PFHxS. Conversely, the 95% CI of t_a ranges from 0.7 to 4.5 years for PFBS, 0.9 to 6 years for PFPeA. The wide range of uncertainties shown in the model predictions resulting from the parameter uncertainties implies that it is important to quantify the uncertainty when limited information and parameters are available at contamination sites, especially for the long-chain PFAS. The distribution of the arrival times computed from the Monte Carlo simulations also illustrates that—depending on the specific parameters employed in the simulations—the arrival time for a certain PFAS can vary by one or two orders of magnitude even within the 95% CI. This again suggests that it is critical to quantify the uncertainty associated with any numerical predictions especially when the input parameters are uncertain.

The log-normal distributions of the arrival times t_a may be caused by the parameters that follow lognormal distributions, i.e., α , α_L , and K_s . Based on the Morris sensitivity analysis in Section 3.2.1, we speculate that the parameter α is likely most responsible for the log-normal distributions of t_a for the longchain PFAS, for which AWIA dominates the retention (except for PFTrDA). For the short-chain PFAS and PFTrDA, both the parameters α and α_L are primary controls on PFAS leaching.

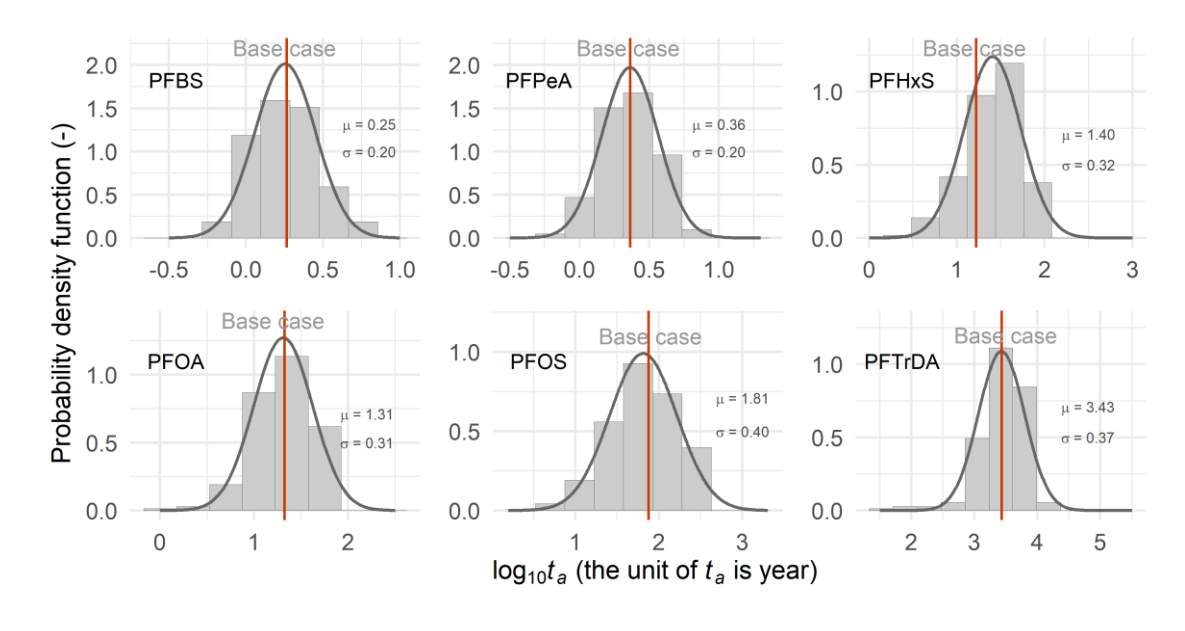


Figure 11. The probability density function of the logarithmic arrival time t_a for each PFAS obtained from the Monte Carlo simulations. In the random realizations, there are 11 parameters randomly perturbed within the designated uncertainty ranges, namely, σ_0 , a, b, $\log K_s$, θ_s , θ_r , $\log \alpha$, n, $\log \alpha_L$, K_f , and N. The results are fitted to log-normal distributions. Note that the arrival time for PFTrDA, which can be much longer than the simulated period, is estimated as the length scale of the domain divided by the mean migration speed of the plume fronts.

3.3 Assumptions and limitations

In this section, we summarize the assumptions employed in our study and discuss their potential impact on PFAS leaching in the vadose zone. The model simulations have not accounted for interactions (e.g., competitive adsorption) among PFAS, hydrocarbon surfactants, and co-solvents in AFFF, change of contact angle between porewater and soil grain surfaces, the dependence of SPA on solution chemistry, the transformation of PFAS precursors, and soil heterogeneity. We discuss each of these assumptions below and identify their impact on the long-term retention of PFAS in the vadose zone.

Interactions among different PFAS can potentially deviate their behavior from what would be observed as a single PFAS. An example would be competitive adsorption at solid—water and air—water interfaces. Guelfo and Higgins (2013) show that competitive SPA is minor for multiple PFAS below the concentration of 1 mg/L for the PFAS and porous media tested. Our simulated maximum *C* is lower than 3.8 mg/L for PFOS for all scenarios and is much lower for other PFAS. The actual aqueous concentrations are relatively low because most of the mass is adsorbed either at solid—water and air—water interfaces. The presence of PFAS mixtures can also influence surface tension and AWIA, though limited data are available in the literature. Vecitis et al. (2008) reported surface tension data for a 1:1 mixture of PFOS and PFOA and Brusseau & Van Glubt (2019) presented surface tension data for a mixture of PFOA and PFTrDA with ratios of 8:2 and 2:8. More comprehensive surface tension data for multiple PFAS mixtures were recently reported by Silva et al (2021). All of the studies showed that the PFAS with greater surface activity dominates the overall surface activity of the mixture. Our model simulations do not consider interactions among PFAS mixtures and other hydrocarbon surfactants or co-solvents. The impact of such interactions on PFAS retention and leaching will depend upon the nature and magnitude of the interactions (Huang et al., 2021; Ji et al., 2021).

Interaction between soil grain surfaces and chemical components (i.e., PFAS, hydrocarbon surfactants, or co-solvents) can also increase the contact angle of porewater at the soil grain surfaces, especially for the cationic, zwitterionic, or nonionic surfactants. To date, no experimental data for the dependence of contact angle on the aqueous concentration of PFAS have been reported. Measured data for other surfactants are also limited (Desai et al., 1992). The change of contact angle by PFAS may be quantified when experimental data become available. Similarly, the impact of solution chemistry on SPA is not considered in our model simulations presented in Section 3.1.1 due to a lack of measured data. The impact of solution chemistry on PFAS SPA will depend on the properties of the PFAS and the soil.

PFAS precursors are important components of many AFFF concentrates (e.g., Houtz et al., 2013) and they can be transformed through either biotic or abiotic reactions to PFSAs and PFCAs in the environment (e.g., Avendano and Liu, 2015). We have not accounted for these transformations in the present work, but our modeling framework can be extended to include transformations of precursors when detailed reaction pathways and kinetics become available in the future.

The non-Fickian transport caused by immobile water observed in several prior experimental and numerical studies for non-PFAS solutes under water-unsaturated conditions (e.g., De Gennes, 1983; Hasan et al., 2020; Padilla et al., 1999; Raoof & Hassanizadeh, 2013; Stults et al., 2021), has not been considered in our study. This immobile-water-caused non-Fickian behavior could be an important factor that can influence long-term PFAS leaching, especially at relatively lower water saturation.

Finally, soil heterogeneity (such as soil layering, macropores, and fractures) may strongly influence PFAS leaching in the vadose zone. We considered vadose zones represented by homogeneous soils to focus on analyzing the physical and chemical processes influencing retention. Future investigations are needed to fully delineate the impact of soil heterogeneity on PFAS leaching, which may strongly influence the long-term leaching as suggested by Zeng & Guo (2021).

4 Conclusion

We present a modeling study that focuses on analyzing the primary processes and parameters controlling the long-term PFAS leaching and retention in the vadose zone. We first use multiple experimental data sets to validate a mathematical model that represents variably saturated flow, surfactant-induced flow, advection, dispersion, as well as nonlinear and rate-limited adsorption of PFAS at the soil—water and air—water interfaces. Then, we employ the validated mathematical model to investigate the primary factors and parameters controlling the long-term leaching and retention behavior by conducting simulations and parameter sensitivity and uncertainty analyses under a wide range of conditions. Our specific conclusions are summarized below:

- (1) The long-term retention and leaching of PFAS in the vadose zone are primarily controlled by chain length, soil properties, solution chemistry, and the applied concentration. Due to enhanced SPA and AWIA, PFAS retention in the vadose zone increases for longer-chain PFAS, higher ionic strengths, and lower applied concentrations.
- (2) Parameter sensitivity analysis reveals that the parameters to which the model simulations are most sensitive differ among different PFAS. The rank of these parameters (i.e., relative sensitivity) is mainly controlled by the relative importance of SPA and AWIA. When SPA is more important, the model predictions are most sensitive to parameters for SPA (especially the Freundlich exponent *N*) due to its nonlinearity. Conversely, when AWIA is dominant (e.g., for long-chain PFAS at relatively greater concentrations, e.g., PFHxS, PFOA, and PFOS), the model predictions are most sensitive to parameters related to the air—water interfacial area and PFAS interfacial properties. Dispersivity is a primary parameter for all PFAS as it controls the overall spreading of the plume.
- (3) Parameter uncertainty analysis suggests that the model simulations involve a wide range of uncertainties due to uncertainties propagated from the model parameters. The time for PFAS to break through (i.e., arrival time) appears to follow log-normal distributions for all PFAS. However, the uncertainty range is much greater for longer-chain PFAS compared to that of their shorter-chain

counterparts. This suggests that it is important to quantify uncertainties for the simulated PFAS leaching when limited site information and parameters are available at contamination sites, especially for the long-chain PFAS.

- (4) Nonlinearity in AWIA is insignificant under the field conditions examined in the present study and may be simplified for practical application at many legacy PFAS contamination sites. Because the AFFF-impacted FTA sites are among the contamination sites that have the highest PFAS concentrations, assuming linear AWIA is expected to be even more appropriate for other contamination sites with lower PFAS concentrations such as agricultural lands that received PFAS-contaminated biosolids and irrigation water.
- (5) Both kinetic SPA and kinetic AWIA are generally insignificant under the field conditions examined in the present study. We note that the importance of kinetic SPA and kinetic AWIA was only determined based on kinetic parameters obtained for a limited number of miscible-displacement experiments conducted in a sand media and field-contaminated soil samples from only one historical AFFF-impacted site. Therefore, the general importance of kinetic SPA and kinetic AWIA under a wider range of conditions for different kinds of field-contaminated sites and different PFAS needs further investigation.

Acknowledgments

This work is in part supported by the National Science Foundation (2023351), the Environmental Security
Technology Certification Program (Project ER21-5041), and the NIEHS Superfund Research Program
(grant # P42 ES 4940).

References

- Adamson, A.W., Gast, A.P., 1997. Physical Chemistry of Surfaces, 6th ed. John Wiley & Sons, Inc., New York.
- Adamson, D.T., Nickerson, A., Kulkarni, P.R., Higgins, C.P., Popovic, J., Field, J., Rodowa, A., Newell, C., DeBlanc, P. and Kornuc, J.J., 2020. Mass-Based, Field-Scale Demonstration of PFAS Retention within AFFF-Associated Source Areas. Environmental Science & Technology. https://doi.org/10.1021/acs.est.0c04472
 - An, S.W., Lu, J.R., Thomas, R.K. and Penfold, J., 1996. Apparent anomalies in surface excesses determined from neutron reflection and the Gibbs equation in anionic surfactants with particular reference to perfluorooctanoates at the air/water interface. Langmuir, 12(10), pp.2446-2453. https://doi.org/10.1021/la950851y
 - Anderson, R., Adamson, D.T., Stroo, H.F., 2019. Partitioning of poly- and perfluoroalkyl substances from soil to groundwater within aqueous film-forming foam source zones. J. Contam. Hydrol. 220, 59–65. https://doi.org/10.1016/j.jconhyd.2018.11.011
- https://doi.org/10.1016/j.jconhyd.2018.11.011

 APEX, 2017. Final report: Preliminary Assessment Aqueous Film-Forming Foam Use Portland International Airport Portland,
 Oregon. Available online: https://www.deq.state.or.us/Webdocs/Controls/Output/PdfHandler.ashx?p=4079b1d7-f8b6-4343-b701-e739287b8357.pdf&s=Preliminary%20Assessment%20Aqueous%20Film-Forming%20Foam%20Use%20PDX%2020170803.pdf
 - Araujo, J. B., Mainhagu, J., & Brusseau, M. L. 2015. Measuring air—water interfacial area for soils using the mass balance surfactant-tracer method. Chemosphere, 134, 199–202. https://doi.org/10.1016/j.chemosphere.2015.04.035

- Arvaniti, O.S., Stasinakis, A.S., 2015. Review on the occurrence, fate and removal of perfluorinated compounds during 862 wastewater treatment. Sci. Total Environ. 524-525, 81-92. https://doi.org/10.1016/j.scitotenv.2015.04.023 863
- Avendano, S.M., Liu, J., 2015. Production of PFOS from aerobic soil biotransformation of two perfluoroalkyl sulfonamide 864 derivatives. Chemosphere 119, 1084–1090. https://doi.org/10.1016/j.chemosphere.2014.09.059 865
 - Baduel, C., Mueller, J.F., Rotander, A., Corfield, J., Gomez-Ramos, M.J., 2017. Discovery of novel per- and polyfluoroalkyl substances (PFASs) at a fire fighting training ground and preliminary investigation of their fate and mobility. Chemosphere 185, 1030–1038. https://doi.org/10.1016/j.chemosphere.2017.06.096
 - Bashir, R., Smith, J.E., Stolle, D.F.E., 2018. Surfactant flow and transport in the vadose zone: a numerical experiment. Environ. Geotech. 1–12. https://doi.org/10.1680/jenge.17.00090
 - Bear, J., 1972. Dynamics of fluids in porous media. Dover Publ., Inc.

867

868

869

870

871

872

873 874

875

876

877 878

879

880

881

882

883

884

885

886

887

888

889

890 891

892

893

894 895

896

897

898

899

900

901

902

903

904

905

906 907

908

909

910

911

912

913

914

915

917

- Buck, R.C., Franklin, J., Berger, U., Conder, J.M., Cousins, I.T., Voogt, P. De, Jensen, A.A., Kannan, K., Mabury, S.A., van Leeuwen, S.P.J., 2011. Perfluoroalkyl and polyfluoroalkyl substances in the environment: Terminology, classification, and origins. Integr. Environ. Assess. Manag. 7, 513-541. https://doi.org/10.1002/ieam.258
- Bradford, S.A. and Leij, F.J., 1997. Estimating interfacial areas for multi-fluid soil systems. Journal of Contaminant Hydrology, 27(1-2), pp.83-105. https://doi.org/10.1016/S0169-7722(96)00048-4
- Bradford, S.A., Wang, Y., Torkzaban, S. and Šimůnek, J., 2015. Modeling the release of E. coli D21g with transients in water content. Water Resources Research, 51(5), pp.3303-3316. https://doi.org/10.1002/2014WR016566
- Brusseau, M.L., 1995. The effect of nonlinear sorption on transformation of contaminants during transport in porous media. Journal of Contaminant Hydrology, 17(4), 277-291. https://doi.org/10.1016/0169-7722(94)00041-F
- Brusseau, M.L., 2018. Assessing the potential contributions of additional retention processes to PFAS retardation in the subsurface. Sci. Total Environ. 613-614, 176-185. https://doi.org/10.1016/j.scitotenv.2017.09.065
- Brusseau, M.L., 2019a. The influence of molecular structure on the adsorption of PFAS to fluid-fluid interfaces: using QSPR to predict interfacial adsorption coef- ficients. Water Res. 152, 148-158. https://doi.org/10.1016/j.watres.2018.12.057
- Brusseau, M.L., 2019b. Estimating the relative magnitudes of adsorption to solid-water and air/oil-water interfaces for per-and poly-fluoroalkyl substances. Environ. Pollut. 254, 113102. https://doi.org/10.1016/j.envpol.2019.113102
- Brusseau, M.L., 2020. Simulating PFAS transport influenced by rate-limited multi-process retention. Water Res. 168, https://doi.org/10.1016/j.watres.2019.115179
- Brusseau, M.L., 2021. Examining the robustness and concentration dependency of PFAS air-water and NAPL-water interfacial adsorption coefficients. Water research, 190, p.116778, https://doi.org/10.1016/j.watres.2020.116778
- Brusseau, M.L., Anderson, R.H., Guo, B., 2020a. PFAS concentrations in soils: Background levels versus contaminated sites. Sci. Total Environ. 740, 140017. https://doi.org/10.1016/j.scitotenv.2020.140017
- Brusseau, M. L., El Ouni, A., Araujo, J. B., & Zhong, H. 2015. Novel methods for measuring air-water interfacial area in unsaturated porous media. Chemosphere, 127, 208-213. https://doi.org/10.1016/j.chemosphere.2015.01.029
- Brusseau, M. L., Guo, B., 2021. Air-Water Interfacial Areas Relevant for Transport of Per and Poly-Fluoroalkyl Substances. Water Res. https://doi.org/10.1016/j.watres.2021.117785 (In press)
- Brusseau, M.L., Guo, B., Huang, D., Yan, N. and Lyu, Y., 2021. Ideal versus Nonideal Transport of PFAS in Unsaturated Porous Media. Water Research, p.117405. https://doi.org/10.1016/j.watres.2021.117405
- Brusseau, M.L., Khan, N., Wang, Y., Yan, N., Van Glubt, S., Carroll, K.C., 2019a. Nonideal Transport and Extended Elution Tailing of PFOS in Soil. Environ. Sci. Technol. 53, 10654–10664. https://doi.org/10.1021/acs.est.9b02343
- Brusseau, M.L, Lyu, Y., Yan, N., Guo, B., 2020b. Low-concentration tracer tests to measure air-water interfacial area in porous media. Chemosphere 250, 126305. https://doi.org/10.1016/j.chemosphere.2020.126305
- Brusseau, M.L., Peng, S., Schnaar, G. and Murao, A., 2007. Measuring air-water interfacial areas with x-ray microtomography and interfacial partitioning tracer tests. Environmental science & technology, 41(6), pp.1956-1961. https://doi.org/10.1021/es061474m
- Brusseau, M.L., Van Glubt, S., 2019. The influence of surfactant and solution composition on PFAS adsorption at fluid-fluid interfaces. Water Res. 161, 17-26. https://doi.org/10.1016/j.watres.2019.05.095
- Brusseau, M.L, Yan, N., Van Glubt, S., Wang, Y., Chen, W., Lyu, Y., Dungan, B., Carroll, K.C., Holguin, F.O., 2019b. Comprehensive retention model for PFAS transport in subsurface systems. Water Res. 148, 41-50. https://doi.org/10.1016/j.watres.2018.10.035
- Cameron, D., & Klute, A. (1977). Convective-dispersive solute transport with a combined equilibrium and kinetic adsorption model. Water Resources Research, 13(1), 183-188. https://doi.org/10.1029/WR013i001p00183
- Campbell, T.Y., Vecitis, C.D., Mader, B.T., Hoffmann, M.R., 2009. Perfluorinated Surfactant Chain-Length Effects on Sonochemical Kinetics. J. Phys. Chem. A 113, 9834–9842. https://doi.org/10.1021/jp903003w
- Campolongo, F., Kleijnen, J., Andres, T., 2000. Screening methods. In: Saltelli, A., Chan, K., Scott, E.M. (Eds.), Sensitivity 916 Analysis. Wiley, Chichester, England, pp. 65–80.
 - Campolongo, F., Cariboni, J. and Saltelli, A., 2007. An effective screening design for sensitivity analysis of large models. Environmental modelling & software, 22(10), pp.1509-1518. https://doi.org/10.1016/j.envsoft.2006.10.004
- Casson, R., Chiang, S.Y.D., 2018. Integrating total oxidizable precursor assay data to evaluate fate and transport of PFASs. 919 Remediation 28, 71–87. https://doi.org/10.1002/rem.21551 920
- Chang, C.H., Franses, E.I., 1995. Adsorption dynamics of surfactants at the air/water interface: a critical review of mathematical 921 models, data, and mechanisms. Colloids Surfaces A Physicochem. Eng. Asp. 100, 1-45. https://doi.org/10.1016/0927-922 7757(94)03061-4 923

- Chen, J., Yan, Peng., Chen, W., Jin-Xin, X., 2005. Effect of counterions on fluorinated surfactants. Acta Chimica Sinica 63, 279-282.
- 926 Clark, K., 2004. AmeriFlux US-Slt Silas Little-New Jersey (Tech. Rep.). http://www.nrs.fs.fed.us/ef/locations/nj/silas-little/
- Costanza, J., Arshadi, M., Abriola, L.M., Pennell, K.D., 2019. Accumulation of PFOA and PFOS at the Air--Water Interface. Environ. Sci. Technol. Lett. 6, 487–491. https://doi.org/10.1021/acs.estlett.9b00355
 - Costanza, J., Abriola, L.M. and Pennell, K.D., 2020. Aqueous Film-Forming Foams Exhibit Greater Interfacial Activity than PFOA, PFOS, or FOSA. Environmental Science & Technology, 54(21), pp.13590-13597. https://doi.org/10.1021/acs.est.0c03117
 - Costello, M.C.S. and Lee, L.S., 2020. Sources, fate, and plant uptake in agricultural systems of per-and polyfluoroalkyl substances. Current Pollution Reports, pp.1-21. https://doi.org/10.1007/s40726-020-00168-y

- Cousins, I.T., DeWitt, J.C., Glüge, J., Goldenman, G., Herzke, D., Lohmann, R., Miller, M., Ng, C.A., Scheringer, M., Vierke, L. and Wang, Z., 2020. Strategies for grouping per-and polyfluoroalkyl substances (PFAS) to protect human and environmental health. Environmental Science: Processes & Impacts, 22(7), pp.1444-1460. https://doi.org/10.1039/D0EM00147C
 - Dauchy, X., Boiteux, V., Colin, A., Hémard, J., Bach, C., Rosin, C., Munoz, J.F., 2019. Deep seepage of per- and polyfluoroalkyl substances through the soil of a firefighter training site and subsequent groundwater contamination. Chemosphere 214, 729–737. https://doi.org/10.1016/j.chemosphere.2018.10.003
 - De Gennes, P. G. 1983. Hydrodynamic Dispersion in Unsaturated Porous Media. J. Fluid Mech. 136, 189-200. https://doi.org/10.1017/S0022112083002116
- Downes, N., Ottewill, G.A. and Ottewill, R.H., 1995. An investigation of the behaviour of ammonium perfluoro-octanoate at the air/water interface in the absence and presence of salts. Colloids and Surfaces A: Physicochemical and Engineering Aspects, 102, pp.203-211. https://doi.org/10.1016/0927-7757(95)03191-F
 - Dmowski, W., 1990. Synthetic utility of 3-(perfluoro-1, 1-dimethylbutyl)-1-propene. Part IV. Synthesis and properties of 1, 1, 1, 2, 2, 3, 3, 8, 9, 9, 9-undecafluoro-4, 4, 8-tris (trifluoromethyl) nonane-a new potential oxygen carrier for biomedical use. Journal of fluorine chemistry, 50(3), pp.319-325. https://doi.org/10.1016/S0022-1139(00)84997-0
- El Ouni, A., Guo, B., Zhong, H., Brusseau, M.L., 2021. Testing the validity of the miscible-displacement interfacial tracer method for measuring air—water interfacial area: Independent benchmarking and mathematical modeling. Chemosphere 263, 128193. https://doi.org/10.1016/j.chemosphere.2020.128193
 - FAA, 2010. Advisory circular: Aircraft Rescue and Fire Fighting (ARFF) Training Facilities. AC 150/5220-17B-17B
- Filipovic, M., Woldegiorgis, A., Norström, K., Bibi, M., Lindberg, M., Österås, A.H., 2015. Historical usage of aqueous film forming foam: A case study of the widespread distribution of perfluoroalkyl acids from a military airport to groundwater, lakes, soils and fish. Chemosphere 129, 39–45. https://doi.org/10.1016/j.chemosphere.2014.09.005
- Gallen, C., Eaglesham, G., Drage, D., Nguyen, T.H., Mueller, J.F., 2018. A mass estimate of perfluoroalkyl substance (PFAS) release from Australian wastewater treatment plants. Chemosphere 208, 975–983. https://doi.org/10.1016/j.chemosphere.2018.06.024
- Garcia, R.A., Chiaia-Hernández, A.C., Lara-Martin, P.A., Loos, M., Hollender, J., Oetjen, K., Higgins, C.P., Field, J.A., 2019. Suspect Screening of Hydrocarbon Surfactants in AFFFs and AFFF-Contaminated Groundwater by High-Resolution Mass Spectrometry. Environ. Sci. Technol. 53, 8068–8077. https://doi.org/10.1021/acs.est.9b01895
- Gottschall, N., Topp, E., Edwards, M., Payne, M., Kleywegt, S., Lapen, D.R., 2017. Brominated flame retardants and perfluoroalkyl acids in groundwater, tile drainage, soil, and crop grain following a high application of municipal biosolids to a field. Sci. Total Environ. 574, 1345–1359. https://doi.org/10.1016/j.scitotenv.2016.08.044
- Guelfo, J.L., Higgins, C.P., 2013. Subsurface transport potential of perfluoroalkyl acids at aqueous film-forming foam (AFFF)-impacted sites. Environ. Sci. Technol. 47, 4164–4171. https://doi.org/10.1021/es3048043
- Guo, B., Zeng, J., Brusseau, M.L., 2020. A Mathematical Model for the Release, Transport, and Retention of Per- and Polyfluoroalkyl Substances (PFAS) in the Vadose Zone. Water Resour. Res. 56, 2019WR026667. https://doi.org/10.1029/2019WR026667
- Hasan, S.; Niasar, V.; Karadimitriou, N. K.; Godinho, J. R. A.; Vo, N. T.; An, S.; Rabbani, A.; Steeb, H. Direct Characterization of Solute Transport in Unsaturated Porous Media Using Fast X-Ray Synchrotron Microtomography. Proc. Natl. Acad. Sci. U. S. A. 2020, 117 (38), 23443-23449. https://doi.org/10.1073/pnas.2011716117
- Hatton, J., Holton, C. and DiGuiseppi, B., 2018. Occurrence and behavior of per-and polyfluoroalkyl substances from aqueous film-forming foam in groundwater systems. Remediation Journal, 28(2), pp.89-99. https://doi.org/10.1002/rem.21552
- Henry, E.J., Smith, J.E., Warrick, A.W., 2001. Surfactant effects on unsaturated flow in porous media with hysteresis: horizontal column experiments and numerical modeling. J. Hydrol. 245, 73–88. https://doi.org/10.1016/S0022-1694(01)00338-9
- Higgins, C.P. and Luthy, R.G., 2006. Sorption of perfluorinated surfactants on sediments. Environmental science & technology, 40(23), pp.7251-7256. https://doi.org/10.1021/es061000n
- Høisæter, Å., Pfaff, A., Breedveld, G.D., 2019. Leaching and transport of PFAS from aqueous film-forming foam (AFFF) in the unsaturated soil at a firefighting training facility under cold climatic conditions. J. Contam. Hydrol. 222, 112–122. https://doi.org/10.1016/j.jconhyd.2019.02.010
- Houtz, E.F., Higgins, C.P., Field, J.A., Sedlak, D.L., 2013. Persistence of perfluoroalkyl acid precursors in AFFF-impacted
 groundwater and soil. Environ. Sci. Technol. 47, 8187–8195. https://doi.org/10.1021/es4018877
- Huang, D., Saleem, H., Guo, B. and Brusseau, M.L., 2021. The impact of multiple-component PFAS solutions on fluid-fluid interfacial adsorption and transport of PFOS in unsaturated porous media. Science of The Total Environment, p.150595. https://doi.org/10.1016/j.scitotenv.2021.150595

- 986 ITRC, 2018. Environmental Fate and Transport for Per- and Polyfluoroalkyl Substances. Washington DC, USA. https://pfas-1.itrcweb.org/fact_sheets page
- Janczuk, B., Bruque, J.M., Gonzalez-Martin, M.L. and Dorado-Calasanz, C., 1995. The adsorption of Triton X-100 at the air-aqueous solution interface. Langmuir, 11(11), pp.4515-4518. https://doi.org/10.1021/la00011a055
 - Ji, Y., Yan, N., Brusseau, M.L., Guo, B., Zheng, X., Dai, M., Liu, H. and Li, X., 2021. Impact of a Hydrocarbon Surfactant on the Retention and Transport of Perfluorooctanoic Acid in Saturated and Unsaturated Porous Media. Environmental Science & Technology. https://doi.org/10.1021/acs.est.1c01919
 - Karagunduz, A., Young, M.H., Pennell, K.D., 2015. Influence of surfactants on unsaturated water flow and solute transport. Water Resour. Res. 51, 1977–1988. https://doi.org/10.1002/2014WR015845
 - Kissa, E., 2001. Fluorinated surfactants and repellents. CRC Press.

991

992

993

994

995

996

997 998

999

1000

1001

1002

1003

1004

1005

1006

1007

1008

1009

1010

1011

1012

1013 1014

1015

1016

1017

1022

1023

1024

1025

1029

1030

1031

1032

1033

1034

1037

- Leverett, M.C., 1941. Capillary behavior in porous solids. Trans. AIME 142, 152-169. https://doi.org/10.2118/941152-G
- Li, F., Fang, X., Zhou, Z., Liao, X., Zou, J., Yuan, B. and Sun, W., 2019. Adsorption of perfluorinated acids onto soils: Kinetics, isotherms, and influences of soil properties. Science of the total environment, 649, pp.504-514. https://doi.org/10.1016/j.scitotenv.2018.08.209
- Li, Z., Lyu, X., Gao, B., Xu, H., Wu, J. and Sun, Y., 2021. Effects of ionic strength and cation type on the transport of perfluorooctanoic acid (PFOA) in unsaturated sand porous media. Journal of Hazardous Materials, 403, p.123688. https://doi.org/10.1016/j.jhazmat.2020.123688
- López-Fontán, J.L., Sarmiento, F. and Schulz, P.C., 2005. The aggregation of sodium perfluorooctanoate in water. Colloid and Polymer Science, 283(8), pp.862-871. https://doi.org/10.1007/s00396-004-1228-7
- Lunkenheimer, K., Prescher, D., Hirte, R., Geggel, K., 2015. Adsorption properties of surface chemically pure sodium perfluoron-alkanoates at the air/water interface: Counterion effects within homologous series of 1:1 ionic surfactants. Langmuir 31, 970-981. https://doi.org/10.1021/la503450k
- Lunkenheimer, K., Geggel, K., Prescher, D., 2017. Role of counterion in the adsorption behaviour of 1:1 ionic surfactants at fluid interfaces Adsorption properties of alkali perfluoro-n-octanoates at the air/water interface. Langmuir 33, 10216-10224. https://doi.org/10.1021/acs.langmuir.7b00786
- Lyu, X., Liu, X., Sun, Y., Gao, B., Ji, R., Wu, J., & Xue, Y. 2020. Importance of surface roughness on perfluorooctanoic acid (PFOA) transport in unsaturated porous media. Environmental Pollution, 266, 115343. https://doi.org/10.1016/j.envpol.2020.115343
- Lyu, Y., Brusseau, M.L., 2020. The influence of solution chemistry on air—water interfacial adsorption and transport of PFOA in unsaturated porous media. Sci. Total Environ. 713, 136744. https://doi.org/10.1016/j.scitotenv.2020.136744
- Lyu, Y., Brusseau, M.L., Chen, W., Yan, N., Fu, X., Lin, X., 2018. Adsorption of PFOA at the air–water interface during transport in unsaturated porous media. Environ. Sci. Technol. 52, 7745–7753. https://doi.org/10.1021/acs.est.8b02348
- Millington, R.J., Quirk, J.P., 1961. Permeability of porous solids. Trans. Faraday Soc. 57, 1200–1207.
 https://doi.org/10.1039/TF9615701200
- Moody, C.A., Field, J.A., 2000. Perfluorinated Surfactants and the Environmental Implications of Their Use in Fire-Fighting Foams. Environ. Sci. Technol. 34, 3864–3870. https://doi.org/10.1021/es991359u
 - Moody, C.A., Field, J.A., 1999. Determination of perfluorocarboxylates in groundwater impacted by fire-fighting activity. Environ. Sci. Technol. 33, 2800–2806. https://doi.org/10.1021/es981355+
 - Morris, M.D., 1991. Factorial sampling plans for preliminary computational experiments. Technometrics, 33(2), pp.161-174. https://doi.org/10.1080/00401706.1991.10484804
- Mualem, Y., 1976. A new model for predicting the hydraulic conductivity of unsaturated porous media. Water Resour. Res. 12, 513–522. https://doi.org/10.1029/WR012i003p00513
 Naidu, R., Nadebaum, P., Fang, C., Cousins, I.T., Pennel, K., Conder, J., Newell, C.J., Longpré, D., Warner, S., Crosbie, N.D.
 - Naidu, R., Nadebaum, P., Fang, C., Cousins, I.T., Pennel, K., Conder, J., Newell, C.J., Longpré, D., Warner, S., Crosbie, N.D. and Surapaneni, A., 2020. Per-and poly-fluoroalkyl substances (PFAS) current status and research needs. https://doi.org/10.1016/j.eti.2020.100915
 - OECD, 2018. Toward a New Comprehensive Global Database of Per-and Polyfluoroalkyl Substances (PFASs): Summary Report on Updating the OECD 2007 List of per-and Polyfluoroalkyl Substances (PFASs). Contract No.: JT03431231
 - Padilla, I. Y.; Yeh, T. C. J.; Conklin, M. H. The Effect of Water Content on Solute Transport in Unsaturated Porous Media. Water Resour. Res. 1999, 35 (11), 3303-3313. https://doi.org/10.1029/1999WR900171
- Place, B.J., Field, J.A., 2012. Identification of novel fluorochemicals in aqueous film-forming foams used by the US military. Environ. Sci. Technol. 46, 7120–7127. https://doi.org/10.1021/es301465n
 - Raoof, A., & Hassanizadeh, S. M. 2013. Saturation-dependent solute dispersivity in porous media: Pore-scale processes. Water Resources Research, 49(4), 1943–1951. https://doi.org/10.1002/wrcr.20152
- Richards, L.A., 1931. Capillary conduction of liquids through porous mediums. J. Appl. Phys. 1, 318–333. https://doi.org/10.1063/1.1745010
- Richardson, L.F., 1921. Weather prediction by numerical process. Cambridge university press.
- Rosen, M.J., Kunjappu, J.T., 2012. Surfactants and Interfacial Phenomena, Surfactants and Interfacial Phenomena: Fourth Edition. John Wiley & Sons, Inc., Hoboken, NJ, USA. https://doi.org/10.1002/9781118228920
- Rotander, A., Toms, L.M.L., Aylward, L., Kay, M. and Mueller, J.F., 2015. Elevated levels of PFOS and PFHxS in firefighters exposed to aqueous film forming foam (AFFF). Environment international, 82, pp.28-34. https://doi.org/10.1016/j.envint.2015.05.005

- Russo, D. and Bouton, M., 1992. Statistical analysis of spatial variability in unsaturated flow parameters. Water Resources Research, 28(7), pp.1911-1925. https://doi.org/10.1029/92WR00669
- Schaefer, C.E., Culina V, Nguyen D, Field J., 2019a Uptake of poly- and perfluoroalkyl substances at the air–water interface.

 Environ Sci Technol. Nov 5;53(21):12442-12448. https://doi.org/10.1021/acs.est.9b04008
- Schaefer, C.E., Drennan, D.M., Tran, D.N., Garcia, R., Christie, E., Higgins, C.P., Field, J.A., 2019b. Measurement of Aqueous Diffusivities for Perfluoroalkyl Acids. J. Environ. Eng. 145, 06019006. https://doi.org/10.1061/(ASCE)EE.1943-7870.0001585
- Schaefer, C.E., Nguyen, D. and Field, J., 2020. Response to the Comment on "Uptake of Poly-and Perfluoroalkyl Substances at the Air–water Interface". Environmental science & technology, 54(11), pp.7021-7022.
 https://doi.org/10.1021/acs.est.0c02488
 - Schaefer, C.E., Nguyen, D., Christie, E., Shea, S., Higgins, C.P. and Field, J.A., 2021. Desorption of Poly-and Perfluoroalkyl Substances from Soil Historically Impacted with Aqueous Film-Forming Foam. Journal of Environmental Engineering, 147(2), p.06020006. https://doi.org/10.1061/(ASCE)EE.1943-7870.0001846
 - Scott, R., 2004. US-Wkg: Walnut Gulch Kendall Grasslands. https://doi.org/10.17190/AMF/1246112

1058

1059

1060

1063

1064

1065

1066

1067

1068

1069

1070

1071

1072

1073

1074 1075

1076

1077

1078

1081

1082

1083

1084

1085

1086

1087

1088

1089

1090

1091

1092

1093

1094

1095

1096

1097

1098

- Sepulvado, J.G., Blaine, A.C., Hundal, L.S., Higgins, C.P., 2011. Occurrence and fate of perfluorochemicals in soil following the land application of municipal biosolids. Environ. Sci. Technol. 45, 8106–8112. https://doi.org/10.1021/es103903d
 - SERDP, 2017. SERDP and ESTCP Workshop on Research and Demonstration Needs for Management of AFFF-impacted Sites. Department of Defence.
 - Sharifan, H., Bagheri, M., Wang, D., Burken, J.G., Higgins, C.P., Liang, Y., Liu, J., Schaefer, C.E. and Blotevogel, J., 2021. Fate and transport of per-and polyfluoroalkyl substances (PFASs) in the vadose zone. Science of The Total Environment, p.145427. https://doi.org/10.1016/j.scitotenv.2021.145427
 - Shin, H.M., Ryan, P.B., Vieira, V.M., Bartell, S.M., 2012. Modeling the air-soil transport pathway of perfluorooctanoic acid in the mid-Ohio Valley using linked air dispersion and vadose zone models. Atmos. Environ. 51, 67–74. https://doi.org/10.1016/j.atmosenv.2012.01.049
 - Shin, H.M., Vieira, V.M., Ryan, P.B., Detwiler, R., Sanders, B., Steenland, K., Bartell, S.M., 2011. Environmental fate and transport modeling for perfluorooctanoic acid emitted from the Washington works facility in West Virginia. Environ. Sci. Technol. 45, 1435–1442. https://doi.org/10.1021/es102769t
 - Shinoda, K., Hato, M. and Hayashi, T., 1972. Physicochemical properties of aqueous solutions of fluorinated surfactants. The Journal of Physical Chemistry, 76(6), pp.909-914. https://doi.org/10.1021/j100650a021
 - Silva, J.A.K., Martin, W.A., Johnson, J.L., McCray, J.E., 2019. Evaluating air—water and NAPL-water interfacial adsorption and retention of Perfluorocarboxylic acids within the vadose zone. J. Contam. Hydrol. 223, 103472. https://doi.org/10.1016/j.jconhyd.2019.03.004
- Silva, J. A. K., Šimůnek, J., & McCray, J. E. 2020. A Modified HYDRUS Model for Simulating PFAS Transport in the Vadose Zone. Water, 12(10), 2758. https://doi.org/10.3390/w12102758
 - Silva, J.A., Martin, W.A. and McCray, J.E., 2021. Air—water interfacial adsorption coefficients for PFAS when present as a multi-component mixture. Journal of Contaminant Hydrology, 236, p.103731. https://doi.org/10.1016/j.jconhyd.2020.103731
 - Sima, M.W. and Jaffé, P.R., 2020. A critical review of modeling Poly-and Perfluoroalkyl Substances (PFAS) in the soil–water environment. Science of the Total Environment, p.143793. https://doi.org/10.1016/j.scitotenv.2020.143793
 - Simon, J.A., Abrams, S., Bradburne, T., Bryant, D., Burns, M., Cassidy, D., Cherry, J., Chiang, S.-Y., Cox, D., Crimi, M., others, 2019. PFAS Experts Symposium: Statements on regulatory policy, chemistry and analytics, toxicology, transport/fate, and remediation for per-and polyfluoroalkyl substances (PFAS) contamination issues. Remediat. J. 29, 31–48. https://doi.org/10.1002/rem.21624
 - Smith, J.E., Gillham, R.W., 1999. Effects of solute concentration-dependent surface tension on unsaturated flow: Laboratory sand column experiments. Water Resour. Res. 35, 973–982. https://doi.org/10.1029/1998WR900106
 - Smith, J.E., Gillham, R.W., 1994. The effect of concentration-dependent surface tension on the flaw of water and transport of dissolved organic compounds: A pressure head-based formulation and numerical model. Water Resour. Res. 30, 343–354. https://doi.org/10.1029/93WR02745
 - Stults, J.; Illangasekare, T.; Higgins, C. P. The Mass Transfer Index (MTI): A Semi-Empirical Approach for Quantifying Transport of Solutes in Variably Saturated Porous Media. J. Contam. Hydrol. 2021, 242. https://doi.org/10.1016/j.jconhyd.2021.103842
 - Tamaki, K., Ohara, Y. and Watanabe, S., 1989. Solution properties of sodium perfluoroalkanoates. Heats of solution, viscosity B coefficients, and surface tensions. Bulletin of the Chemical Society of Japan, 62(8), pp.2497-2501. https://doi.org/10.1246/bcsj.62.2497
- van Genuchten, M.T., 1980. A Closed-form Equation for Predicting the Hydraulic Conductivity of Unsaturated Soils1. Soil Sci. Soc. Am. J. 44, 892. https://doi.org/10.2136/sssaj1980.03615995004400050002x
- Van Glubt, S., Brusseau, M.L., Yan, N., Huang, D., Khan, N. and Carroll, K.C., 2021. Column versus batch methods for
 measuring PFOS and PFOA sorption to geomedia. Environmental Pollution, 268, p.115917.
 https://doi.org/10.1016/j.envpol.2020.115917
- Vecitis, C.D., Park, H., Cheng, J., Mader, B.T., Hoffmann, M.R., 2008. Enhancement of Perfluorooctanoate and
 Perfluorooctanesulfonate Activity at Acoustic Cavitation Bubble Interfaces. J. Phys. Chem. C 112, 16850–16857.
 https://doi.org/10.1021/jp804050p

- Venkatesan, A.K., Halden, R.U., 2013. National inventory of perfluoroalkyl substances in archived U.S. biosolids from the 2001 EPA National Sewage Sludge Survey. J. Hazard. Mater. 252–253, 413–418. https://doi.org/10.1016/j.jhazmat.2013.03.016
- Washington, J.W., Yoo, H., Ellington, J.J., Jenkins, T.M., Libelo, E.L., 2010. Concentrations, distribution, and persistence of
 perfluoroalkylates in sludge-applied soils near Decatur, Alabama, USA. Environ. Sci. Technol. 44, 8390–8396.
 https://doi.org/10.1021/es1003846
- Weber, A.K., Barber, L.B., Leblanc, D.R., Sunderland, E.M., Vecitis, C.D., 2017. Geochemical and Hydrologic Factors
 Controlling Subsurface Transport of Poly- and Perfluoroalkyl Substances, Cape Cod, Massachusetts. Environ. Sci. Technol.
 51, 4269–4279. https://doi.org/10.1021/acs.est.6b05573
- Xiao, F., Simcik, M.F., Halbach, T.R., Gulliver, J.S., 2015. Perfluorooctane sulfonate (PFOS) and perfluorooctanoate (PFOA) in
 soils and groundwater of a U.S. metropolitan area: Migration and implications for human exposure. Water Res. 72, 64–74.
 https://doi.org/10.1016/j.watres.2014.09.052
- Xu, M., Eckstein, Y., 1995. Use of Weighted Least-Squares Method in Evaluation of the Relationship Between Dispersivity and Field Scale. Groundwater 33, 905–908. https://doi.org/10.1111/j.1745-6584.1995.tb00035.x
- Zeng, J. and Guo, B., 2021. Multidimensional simulation of PFAS transport and leaching in the vadose zone: Impact of surfactant-induced flow and subsurface heterogeneities. Advances in Water Resources, 155, p.104015.
 https://doi.org/10.1016/j.advwatres.2021.104015
- Zhang, Y. and Schaap, M.G., 2017. Weighted recalibration of the Rosetta pedotransfer model with improved estimates of hydraulic parameter distributions and summary statistics (Rosetta3). Journal of Hydrology, 547, pp.39-53.
 https://doi.org/10.1016/j.jhydrol.2017.01.004
- Zhi, Y. and Liu, J., 2018. Sorption and desorption of anionic, cationic and zwitterionic polyfluoroalkyl substances by soil organic matter and pyrogenic carbonaceous materials. Chemical Engineering Journal, 346, pp.682-691.
 https://doi.org/10.1016/j.cej.2018.04.042